Determination of the time-dependent moment tensor using time-reverse imaging

Claudia Finger[*†] **and Erik H. Saenger**[‡*†]

[*] *Fraunhofer IEG, Fraunhofer Reseach Institution for Energy Infrastructure and Geothermal Systems,*

Am Hochschulcampus 1,

44801 Bochum, Germany

[†] *Ruhr-University Bochum,*

Universitätsstr. 150

44801 Bochum, Germany

[‡] *University of Applied Sciences Bochum,*

Am Hochschulcampus 1

44801 Bochum, Germany

(December 10, 2020)

GEO-2020-0348

Running head: **Moment tensors using TRI**

ABSTRACT

An approach is presented to determine the time-dependent moment tensor and the origin time in addition to commonly derived locations of seismic events using time-reverse imaging (TRI). It is crucial to locate and characterize the occurring micro-seismicity without making a priori assumptions about the sources to fully understand the subsurface processes inducing seismicity. Low signal-to-noise ratios often force standard methods to make assumptions about sources or only characterize selected larger-magnitude events. In TRI, micro-earthquakes are located by back propagating the full recorded time-reversed wavefield through a velocity model until it ideally convergences on the source location. Therefore, it is less affected by low signal-to-noise ratios and potentially locates and characterizes most of the events. After distinguishing artificial convergence locations from source locations, the quality of the source location and the moment tensors are derived by recording the stress at the determined source locations during the back propagation of the time-reversed wavefield. A robust workflow is derived using synthetic test cases in a realistic scenario with velocity models that only approximate the true velocity model and/or noisy displacement traces. The influence of a rudimentary velocity model on the source-location accuracy and characterisation is significant. The proposed workflow handles these less-than optimal station distributions and velocity models. Finally, the derived workflow is successfully applied to field data recorded at the geothermal field of Los Humeros, Mexico. Although only a one-dimensional velocity model is currently available, source locations and (time-dependent) moment tensors could be determined for selected events.

INTRODUCTION

The spatio-temporal distribution of micro-seismic events in a geothermal reservoir may reveal the location, the extent and the stress state of existing faults. Furthermore, the determination of moment tensors and thus fault plane solutions indicates dynamic slip behaviour in the subsurface and enables the determination of the local stress regime (Gephart and Forsyth, 1984). This helps distinguish anthropogenically induced and naturally occurring tectonic events (Cesca et al., 2013; Schoenball et al., 2015). Therefore, a thorough analysis of the seismicity in a reservoir before, during and after any on-site activity is crucial for characterising the reservoir (Shapiro et al., 2002) and assessing the potential seismic hazard (Gaucher et al., 2015; Ellsworth et al., 2019).

The most common tools for locating seismic events in geothermal reservoirs are ray-based (Deichmann and Giardini, 2009; Albaric et al., 2014; Ellsworth et al., 2019; Maurer et al., 2020) and thus rely on the identification of individual seismic phases in the recorded passive seismic data traces. This becomes challenging when the signal-to-noise ratio decreases or events occur close in time and space. Methods for determining the moment tensor, such as first-polarity methods (Maurer et al., 2020) or moment tensor inversions (Kim et al., 2011) use the hypocenters determined by ray-based methods (e.g. Aki and Richards, 1980). There is a strong correlation between hypocenter accuracy, and the uncertainty of the moment tensor solution. Furthermore, moment tensors are often restricted to be double-couple (Deichmann and Giardini, 2009; Maurer et al., 2020) and are commonly only determined for a selected number of (large-magnitude) events (Häring et al., 2008; Albaric et al., 2014; Ellsworth et al., 2019). Especially in a geothermal context, the determination of complete moment tensors without any a priori assumptions is crucial since the processes inducing events are not fully understood yet.

Waveform-based methods determine source locations without identifying the seismic phases (Li et al., 2020). Therefore, they are especially well-suited for low signal-to-noise ratios and quasi-simultaneous events. Additionally, no a priori assumptions about the number of sources or the types of sources are made. Time-reverse imaging (TRI), for example, is a waveform-based method that uses the time-reversed wavefield to image the events (Fink et al., 1999; Gajewski and Tessmer, 2005; Saenger, 2011; Nakata and Beroza, 2016). TRI and other waveform-based methods are particularly sensitive to the station distribution and velocity model (Werner and Saenger, 2018; Willacy et al., 2019). Recent developments in waveform-based methods include the joint determination of subsurface velocities and source locations using time-reversal methods (Witten and Shragge, 2017). Although some studies hinted at the possibility to characterize events with TRI (Saenger, 2011; Kremers et al., 2011), most applications focus on locating the events.

TRI may be used to reconstruct the moment tensor of earthquakes. Mathematically, the nth-component of the displacement, recorded at any point at any time $u_n(\mathbf{x}, t)$ can be calculated for a general moment tensor source $M_{ij}(t)$ as (Kawakatsu and Montagner, 2008):

$$u_n(\mathbf{x}, t) = G_{ni,j}(\mathbf{x}, t; \mathbf{x}_0, 0) * M_{ij}(t), \tag{1}$$

where $G_{ni,j}$ stands here for the spatial derivative of the Green's tensor between the source point $\mathbf{x}_0$ and the observation point $\mathbf{x}$. This spatial derivative of the Green's function is necessary to account for the ij-th component of the moment tensor being spatially separated in j-th direction with acting forces of the double-couple point in i-direction. The symbol $(*)$ denotes the convolution in the time domain. Using the strain Green's tensor H as proposed by Zhao et al. (2006):

$$H_{ijn}(\mathbf{x}, t; \mathbf{x}_0, 0) = \frac{1}{2}\left[G_{in,j}(\mathbf{x}, t; \mathbf{x}_0, 0) + G_{jn,i}(\mathbf{x}, t; \mathbf{x}_0, 0)\right], \tag{2}$$

and the spatial reciprocity of the Green's function (Aki and Richards, 1980), the time-reversal operation may be approximated as (Kawakatsu and Montagner, 2008; Gharti et al., 2011):

$$\hat{M}_{ij}(\mathbf{x}_0, t) \approx \sum_{Receivers} H_{ijn}(\mathbf{x}_0, t; \mathbf{x}, 0) * u_n(t_0 - t), \tag{3}$$

with $\hat{M}_{ij}(\mathbf{x}_0, t)$ being the moment tensor obtained at the source location after backpropagating the time-reversed displacement $u_n(t_0 - t)$ from all available receivers.

Practically, the strain Green's tensor may be calculated directly or approximated by numerical simulations. Gharti et al. (2011) and Chambers et al. (2014) compute strain Green's tensor databases to retrieve the moment tensor of a synthetic source. This approach is memory intensive and inflexible in terms of velocity model updates and changing station networks. Therefore, the use of numerical methods to backpropagate the recorded data from the receivers seems to be more suitable.

In this study, the time-dependent moment tensor is derived using TRI based on numerical simulations. After determining the source location with TRI following Finger and Saenger (2020), the components of the stress tensor are recorded at the determined source location. It is shown that the time-dependent stress tensor at a single grid point represents the time-dependent moment tensor of the source initially implemented at this grid point. Since a moment tensor may be determined for each convergence spot in the TRI image volumes, the most crucial step seems to be the robust distinction between artificial convergence locations and true source locations. A technical workflow is presented to locate and characterize the seismic events. The individual steps of the workflow are demonstrated in a realistic synthetic scenario and then applied to field data recorded at the geothermal field of Los Humeros, Mexico.

CHARACTERISING SOURCES IN A HOMOGENEOUS MODEL

Some studies indicate the possibility that TRI image volumes obtained with different imaging conditions may reveal the source radiation pattern (Lokmer et al., 2009; Artman et al., 2010; Saenger, 2011). As demonstrated in this section, this approach is problematic for surface station networks as commonly used to monitor geothermal reservoirs. Alternatively, the determination of the time-dependent moment tensor by recording the local stress components at the source location is investigated.

Forward simulations

A homogeneous cube with a side length of 4 km (Figure 1), a P-wave velocity of $v_\mathrm{P} = 4000\,\mathrm{m\cdot s^{-1}}$, an S-wave velocity of $v_\mathrm{S} = \frac{v_\mathrm{P}}{\sqrt{3}} = 2309\,\mathrm{m\cdot s^{-1}}$ and a density of $\rho = 2393\,\mathrm{kg\cdot m^{-3}}$ is used to demonstrate the concept of the method. The grid spacing is set to $\Delta x = 20\,\mathrm{m}$, the time increment is set to $\Delta t = 0.003\,\mathrm{s}$ and all sides of the model are free surfaces to simulate a solid cube surrounded by air. A rotated staggered-grid finite-difference scheme (Saenger et al., 2000) with a finite-difference order of two in space as well as time is used to solve the full wave equation.

During the forward simulations, the three components of the displacement are recorded using three different receiver networks (Figure 1): (1) 54 receivers with nine receivers distributed evenly on each of the six sides of the cube, (2) 49 receivers uniformly spaced at the top side of the cube, and (3) nine receivers evenly distributed at the top side of the cube.

Simulations are performed with a synthetic source in the center of the cube. A Ricker source wavelet was used which has a central frequency of $f_{\mathrm{c}} = 5\,\mathrm{Hz}$. The six independent moment-tensor components are implemented by scaling the amplitudes of the different source wavelet components and adding them to the stress. The simulation is repeated to model four different moment tensors: an explosion source M_{e}, a strike-slip source M_{S}, a dip-slip source M_{d}, and an arbitrary source M_{r} with one negative moment tensor component.

Time-reversed simulation and application of imaging conditions

The waveforms recorded at the receivers during the forward simulations are reversed in time and re-inserted at the positions they were recorded at. This time-reversed wavefield is back propagated through the same homogeneous velocity model previously used in the forward simulations, and this ideally focuses at the correct source location. Imaging conditions are used to obtain the source image and to derive the source locations. For example, the P-wave energy density imaging condition $\mathbf{I}_{\mathrm{P}}$ is sensitive to the compressional wavefield calculated with the divergence of the displacement $(\nabla \cdot \mathbf{u}(\mathbf{x}, t))$ and the S-wave energy density imaging condition $\mathbf{I}_{\mathrm{S}}$ is sensitive to the shear wavefield calculated with the curl of the displacement $(\nabla \times \mathbf{u}(\mathbf{x}, t))$ (Saenger, 2011):

$$\mathbf{I}_{\mathrm{P}}(\mathbf{x}) = \max_{t \in [0,T]} (\lambda + 2\mu)[\nabla \cdot \mathbf{u}(\mathbf{x}, t)]^2, \tag{4}$$

$$\mathbf{I}_{\mathrm{S}}(\mathbf{x}) = \max_{t \in [0,T]} \mu[\nabla \times \mathbf{u}(\mathbf{x}, t)]^2. \tag{5}$$

λ and μ represent the Lamé parameters, $\mathbf{x}$ the spatial coordinates and t the time increment. The total energy density imaging condition $\mathbf{I}_{\mathrm{e}}$ is generally reported to be most successful in locating different types of sources (Saenger, 2011; Kocur et al., 2016). $\mathbf{I}_{\mathrm{e}}$ is defined as the sum of stresses σ_{ij} times strains ε_{ij} at every model point (Saenger, 2011):

$$\mathbf{I}_{\mathrm{e}}(\mathbf{x}) = \max_{t\in[0,T]} \sum_i \sum_j [\sigma_{ij}(\mathbf{x},t)\varepsilon_{ij}(\mathbf{x},t)]. \tag{6}$$

Source locations may be identified visually or automatically by searching for local maxima in the image volumes obtained using the imaging conditions. Figure 2 shows the TRI image volumes for the three imaging conditions and using the three receiver sets for a strike-slip source (only $M_{xy} \neq 0$) in the center of the cube. A strike-slip source was chosen as one possible anisotropic source mechanism that commonly occurs in geothermal reservoirs.

Locate and characterize synthetic sources by visual inspection

The source location is clearly visible for all three cases in Figure 2 and coincides with the true source location. Using $\mathbf{I}_{\mathrm{e}}$, a single focus point is visible at the true source location, while for $\mathbf{I}_{\mathrm{P}}$ and $\mathbf{I}_{\mathrm{S}}$ a cluster of focus points appears around the true source location. Additionally, high amplitudes occur around the receiver locations for all three receiver sets. The seismic wavefield is only inserted at these discrete points and propagates outwards from these points. Due to interference of the waveforms and geometrical spreading, the amplitudes decrease with increasing distance to the receivers. This is especially pronounced for receiver set C. Later in this study a method is introduced to suppress these artificial high amplitudes.

The images produced with receiver set A (Figures 2a - 2c) reveal a source image where in $\mathbf{I}_{\mathrm{e}}$ (Figure 2a) the source location is well-defined and accurately represents the true source location. In $\mathbf{I}_{\mathrm{P}}$ (Figure 2b) and $\mathbf{I}_{\mathrm{S}}$ (Figure 2c), the characteristic source radiation pattern of four lobes for a strike-slip source (refer, e.g., to Aki and Richards (1980) for a description of the radiation pattern) is visible. Comparing the absolute amplitudes of $\mathbf{I}_{\mathrm{P}}$ and $\mathbf{I}_{\mathrm{S}}$ reveals the dominance of the shear waves. The center of the four focus points in $\mathbf{I}_\mathrm{p}$ and $\mathbf{I}_\mathrm{s}$ is at the true source location.

Receiver set B has a similar number of total receivers as in set A, but all of them are positioned at the top side of the cube. This represents a typical surface seismic network. The source location can be identified in $\mathbf{I}_\mathrm{e}$ (Figure 2d) correctly. However, the focus is elongated in z-direction which may be interpreted as a larger uncertainty in this direction. This can be expected from a station network with limited extent. In $\mathbf{I}_\mathrm{s}$ (Figure 2f), the true source location is at the center of the high amplitudes. However, the source radiation pattern is not reconstructed correctly. In $\mathbf{I}_\mathrm{p}$ (Figure 2e), the source can hardly be located. Locating the source by searching for the highest amplitude in $\mathbf{I}_\mathrm{p}$ and $\mathbf{I}_\mathrm{s}$ would introduce a large error in the source location.

The number of receivers has been drastically reduced for receiver set C. In $\mathbf{I}_\mathrm{p}$ and $\mathbf{I}_\mathrm{s}$ (Figures 2h and 2i) the source location cannot be identified. In $\mathbf{I}_\mathrm{e}$ (Figure 2g) the source location is as visible as when using receiver set B. All information about the source type is lost since no information can be gathered from $\mathbf{I}_\mathrm{p}$ and $\mathbf{I}_\mathrm{s}$. With a heterogeneous velocity structure and noisy data, this effect is expected to be even larger.

With an optimal receiver network and a homogeneous velocity model, the source type can be recovered from the TRI images by comparing the source images produced by different imaging conditions. $\mathbf{I}_\mathrm{e}$ produces accurate source locations with all three receiver sets. $\mathbf{I}_\mathrm{p}$ and $\mathbf{I}_\mathrm{s}$ allow the identification of the source type when using receiver set A but do not allow the characterisation when using the other two receiver sets that only have stations at the top of the cube. Therefore, using receiver set B and C does not allow for a characterization of the source by visual inspection of the images.

Characterize synthetic sources using the stress tensor

The moment tensor components of sources may be approximated by recording the individual stress tensor components at the source location. The moment tensor is defined as the internal forces at a point (e.g., Aki and Richards, 1980) and the stress is defined as the force (F) per area (A) for an infinitesimal area $\sigma_{ij} = \lim_{A \to 0}(\frac{F}{A})$ (e.g., Lowrie, 2007).

The stress tensor at the source location is representative of the moment tensor as demonstrated here by locating four different source types with the three receiver sets each and recording the stress at the initial source location. The recorded stress is plotted time-reversed and scaled in Figure 3 to directly compare it to the initial moment tensor. For this comparison, the moment tensor and the stress were normalised by the largest amplitude in all components so that the amplitude ranges from -1 to 1. For all simulations, the shape and the relative amplitudes of the moment tensor could be perfectly recovered. The noise in the stress traces is minimal for all cases. The inversion of the yy-component for the fourth source type (Figure 3d) can be recovered correctly with all three receiver sets. By picking the maximum amplitudes in Figure 3, the relative scalar moment tensors can be derived from these time-dependent moment tensors. These moment tensors contain all information about the source mechanism. In all cases, the general source type can be recovered, which can also be seen by comparing the focal mechanism solutions plotted for the initial moment tensors and those for the stress tensors produced with receiver set C (Figure 3 bottom).

Using the stress recorded at the source location provides a way of deriving the relative time-dependent moment tensor without any a priori assumptions about the source other than the point source approximation inherent to the moment tensor representation itself.

CHARACTERIZING SOURCES IN A SYNTHETIC REALISTIC SCENARIO

Locating micro-seismic events using TRI encounters challenges when the station network is sparse and irregular (Werner and Saenger, 2018; Franczyk, 2019), the velocity model is complex or erroneous (Steiner et al., 2011; Köhn et al., 2016) and the noise level is high (Witten and Artman, 2011; Werner and Saenger, 2018). A workflow is developed in this study for locating and characterizing seismic events in the presence of these challenges. This workflow is presented in Figure 4 and incorporates the localization of events as proposed by Finger and Saenger (2020) and the characterization of earthquakes using stress recordings at the determined source locations. A crucial step is the distinction between artificial convergence locations and source locations. Synthetic test cases are used to motivate the workflow and common challenges are investigated to outline the robustness of the approach. The results of this section lead to the final workflow presented in Figure 4. In this study, a passive seismic survey over a geothermal reservoir is synthetically reconstructed. Such synthetic studies provide the opportunity to analyse each contribution individually and its overall impact on the final result.

Set-up for a realistic passive seismic survey over a geothermal reservoir

Los Humeros is a geothermal field in the eastern part of the Trans-Mexican Volcanic Belt and is one of two demonstration sites of the EU-funded GeMex project (Jolie et al., 2018). From September 2017 to September 2018, a temporary passive seismic network (Toledo et al., 2019) was installed to monitor natural and potentially induced seismicity and better constrain the subsurface structures. A total of 45 stations were deployed with 27 of them being close to the geothermal plant operated by CFE, a Mexican power company. The positions of these 27 stations are used here as positions for surface receivers (Figure 5).

In Norini et al. (2019), four geological horizons are identified for Los Humeros from well data and structural geologic surveys. The same horizons are interpreted in the one-dimensional velocity model in Löer et al. (2020). This information are combined to create a three-dimensional heterogeneous velocity model with four geologic horizons (Figure 6). During the creation of this three-dimensional heterogeneous model, strong velocity contrasts are created along near-vertical lines to incorporate faults reported in Norini et al. (2019) and Calcagno et al. (2018) as caldera-ring faults.

For the synthetic model, a size of 20 km by 20 km (Figure 5) and a depth of 6 km (Figure 6) is chosen. The grid spacing is set to $\Delta x = 20\,\mathrm{m}$ and the time increment is set to $\Delta t = 0.003\,\mathrm{s}$. This enables the simulation to handle frequencies up to $f_{max} = 15\,\mathrm{Hz}$ without numerical dispersion. The central frequency of the source is set to $f_\mathrm{C} = 5\,\mathrm{Hz}$. Since relative amplitudes are compared when reconstructing the moment tensor, scaling of the magnitude and frequency of the event is neglected. The low-frequency content ensures a smaller model size and hence reduced computational time.

In the first cases, a single synthetic source is placed in the horizon with the second slowest velocity and close to the center of the model (see red star in Figures 5 and 6). The moment tensor of the source is chosen randomly with all components being non-zero and some components being negative. Decomposing the moment tensor after Knopoff and Randall (1970) shows that 21 % are of isotropic (ISO) nature, 69 % are double-couple (DC) and 10 % are compensated linear-vector dipole (CLVD). In some cases, an additional source is added (source 2 in Figure 5) with a pure DC source type and only $M_{xy} \neq 0$. The second source is excited 0.6 s later and deeper than the first one (Figure 5). The seismic waves are propagated from the source through the velocity model using the same finite-difference code as in the previous section and the displacement is recorded at the 27 surface stations that mimic the Los Humeros network. The sides and bottom of the model are absorbing boundaries after Clayton and Engquist (1980) and at the surface the free surface is implemented as vacuum layers. This realistic set-up results in complex displacement traces recorded at the stations (Figure 7a).

Post-processing of TRI image volumes

The only pre-processing step is scaling the amplitudes of each displacement trace by the extrema of the three components of each station so that they are in the range $[-1, 1]$. This was done to homogenize the energy input across stations and counteract geometrical spreading. The recorded traces are time-reversed and back propagated.

In addition to the time-reversed simulation and the application of various imaging conditions, the high amplitudes around the receivers (compare Figure 2) are eliminated using illumination maps as proposed by Witten and Artman (2011). Illumination maps are created by propagating a noise wavefield from the same receivers through the same velocity model as before to highlight parts of the model with high amplitudes from the imaging conditions, such as around receivers or in low-velocity zones. As a noise wavefield, the non-time-reversed traces are used to ensure a similar frequency and amplitude content as the time-reversed data. This wavefield cannot converge at the source location but distributes in the model domain. The image volumes obtained during the time-reversed simulation are then divided by the image volumes of the illumination map, while preventing divisions by zero.

In the illumination compensated volume, the remaining background noise is eliminated by muting amplitudes below a threshold calculated from the mean amplitudes in each coordinate direction as described in detail in Finger and Saenger (2020). The post-processed image volumes for $\mathbf{I}_\mathrm{e}$ can be seen in Figure 8a using the same velocity model in the forward and time-reversed simulation, adding no noise to the displacement traces and using the 27 stations.

The clusters of high amplitudes are identified using an iterative search for the maximum amplitude and subsequently muting the area around it. A detailed description of this approach can be found in Finger and Saenger (2020). The result is a list of convergence points for each tested imaging conditions. The convergence points for $\mathbf{I}_\mathrm{r}$ are shown in Figure 8. For each convergence point, the location in the model, the relative amplitude and the size of the converge location is given. The size is calculated according to Finger and Saenger (2020) by counting non-zero amplitudes in a sphere around the convergence point. The sphere has a radius of twice the minimal S-wave wavelength, calculated as $\lambda_{\mathrm{S},min} = \frac{v_{\mathrm{S},mean}}{f_{max}} = \frac{2658.8\,\mathrm{m/s}}{12\mathrm{Hz}} = 221.57\,\mathrm{m}$ with f_{max} being the maximum frequency of the synthetic source and $v_{\mathrm{S},mean}$ being the mean S-wave velocity of the realistic model. The number of non-zero amplitudes are then converted to a radius assuming the convergence locations are approximately spherical. Note that the size of the convergence spot does not relate to the dimensions of the seismic source. Rather, it can be seen as the quality of convergence. Since an automatic and data-based thresholding method is used, the radii of the convergence locations may be compared. This part of the workflow described in this section is outlined in Figure 4a. Figure 4b and 4c describe subsequent steps that are demonstrated in the following sections.

Typically, an abundance of convergence locations are found. However, only a few sources are usually expected for small time windows. Although the number of sources is known for the synthetic cases, the workflow should work for an unknown number of sources. Therefore, the results are investigated for indicators to distinguish artificial convergence locations from source locations.

Locating and characterising synthetic sources in a realistic scenario

To investigate the most common challenges in geothermal reservoirs on the TRI method, synthetic test cases are set up with and without noisy data and with the true three-dimensional velocity model or a rudimentary one-dimensional velocity model that only approximates the true model. Geothermal reservoirs often experience elevated levels of noise. However, TRI is theoretically capable of locating events with low signal-to-noise ratios (SNR) (Werner and Saenger, 2018). The chosen SNR of one (Figure 7) is too low to reliably pick the onset of seismic phases in the traces (Hardt and Scherbaum, 1994) and thus demonstrates cases in which TRI may be the superior method. Furthermore, for most reservoir applications the determined velocity model may be at least partly incorrect and often only a one-dimensional velocity model is available. Therefore, the influence of using a one-dimensional velocity model (Table 1) in the time-reversed simulation is investigated.

The following experiments are tested for a single source (source 1 in Figures 5 and 6). The first and last tests are repeated with two sources (source 1 and 2 in Figure 5):

1. correct three-dimensional velocity model (Figure 6), no added noise (Figure 7a and 7c) and the 27 surface stations (Figure 5)

2. correct three-dimensional velocity model (Figure 6), added white noise with SNR ~ 1

(Figure 7b) and the 27 surface stations (Figure 5)

3. rudimentary one-dimensional velocity model that approximates the true velocity model (Table 1), no added noise (Figure 7a) and the 27 surface stations (Figure 5)

4. rudimentary one-dimensional velocity model that approximates the true velocity model (Table 1), added white noise with SNR ~ 1 (Figure 7b) and the 27 surface stations (Figure 5)

In all cases investigated, the highest amplitude convergence spot found in $\mathbf{I}_{\mathrm{e}}$ is at the true source location (Figures 8 and 9a). As expected, the convergence locations closest to the true source location in $\mathbf{I}_{\mathrm{S}}$ and $\mathbf{I}_{\mathrm{P}}$ (Figure 9a) are not directly at the source location. $\mathbf{I}_{\mathrm{S}}$ and $\mathbf{I}_{\mathrm{P}}$ seem to image the radiation pattern of the source (compare also Figure 2) and may be zero at the source point location. When assuming that the extension of sources is limited, the proximity of convergence locations found in $\mathbf{I}_{\mathrm{S}}$ and $\mathbf{I}_{\mathrm{P}}$ to those found in $\mathbf{I}_{\mathrm{e}}$ may be used as an indicator for the grade of convergence and hence the source-location accuracy. However, depending on the source type, convergence locations may be more pronounced in $\mathbf{I}_{\mathrm{S}}$ or $\mathbf{I}_{\mathrm{P}}$ or non-existent in one or both of them. Therefore, $\mathbf{I}_{\mathrm{S}}$ and $\mathbf{I}_{\mathrm{P}}$ may be used for initial inspections of the source images, if the velocity structure is not too complex and the station coverage is large. In our field case, $\mathbf{I}_{\mathrm{S}}$ and $\mathbf{I}_{\mathrm{P}}$ are not used in later applications.

The convergence locations found in $\mathbf{I}_{\mathrm{e}}$ are sorted by their relative amplitudes and the amplitudes are plotted in Figure 9b. Only the ten largest-amplitude convergence locations are plotted. The first convergence spot with the highest amplitude is the convergence spot at the true source location for most cases. For the cases using the one-dimensional model, this means that the model is accurate enough in this case to locate sources at the chosen locations. The fourth case repeated with the two sources did not provide a source location in

$\mathbf{I}_\mathrm{e}$ (see Figure 8f) and is not discussed further. For all shown cases, the amplitudes decrease rapidly until the third or fourth convergence spot and stay constant for the remaining spots. The amplitudes are above the threshold level for muting the background in the TRI image volumes for all cases. The magnitude of the decrease in amplitude, called the amplitude drop, may be related to the source-location accuracy. High amplitude drops indicate that the smaller-amplitude convergence points are artifacts. The cases with the correct three-dimensional velocity model experience higher amplitude drops even for noisy data than the cases with the one-dimensional velocity model. This emphasizes that the one-dimensional model is accurate enough to provide source locations, but the accuracy is decreased compared to the three-dimensional model. By identifying the convergence spot where the amplitudes do not decrease anymore, the convergence locations may be separated into source locations and artificial convergence locations. However, the case with two sources demonstrates that the cut-off amplitude should be determined conservatively. The amplitude drops rapidly between the first and second source location and then drops again but less than before.

The radii for the ten largest-amplitude convergence locations found in $\mathbf{I}_\mathrm{e}$ are plotted in Figure 9c in multiples of the minimal S-wave wavelength $\lambda_{\mathrm{S},min}$. These radii are strongly sensitive to the used frequency range. Therefore, providing this value in terms of $\lambda_{\mathrm{S},min}$ allows for a comparison of the quality of the source location. For most cases, the radius of the first convergence spot is the largest of all convergence locations and is between $0.5\,\lambda_{\mathrm{S},min}$ and $1.5\,\lambda_{\mathrm{S},min}$. For the case with the one-dimensional model and noisy data, the radius is below $0.5\lambda_{\mathrm{S},min}$ and do not decrease as rapidly as for the other cases. Zhao et al. (2016) state that generally source locations with TRI cannot be smaller than half the minimal S-wave wavelength due to the diffraction limit. Therefore, very small focus sizes, smaller than $0.5\,\lambda_{\mathrm{S},min}$, are considered to be artificial convergence locations and not source locations. The case with the one-dimensional velocity model and noisy data would be considered unsuccessful although the largest-amplitude convergence spot is at the true source location. Radii larger than $2\lambda_{\mathrm{S},min}$ are non-existent due to the calculation of the focus size as described in the previous section.

The located sources are evaluated using the amplitude drop and the radius (Figure 4). The source locations for the cases with the three-dimensional velocity model are found to be reasonable with and without the noise. The case with the one-dimensional velocity model and noisy data would be categorised as unsuccessful. This demonstrates that the errors introduced by an inadequate velocity model and low signal-to-noise ratios superimpose to hinder successful source locations. The radius is too small and the amplitudes do not decrease rapidly enough to reliably distinguish the source location from artificial convergence locations. The case with the one-dimensional velocity model without noise would be considered ambiguous. In such a case, the TRI image volume (Figure 8c) has to be inspected manually to decide if it is more likely to be a source location or an artificial convergence spot. In this case, it is assumed to be a reasonable source location.

For all investigated cases, the six independent stress-tensor components are recorded at the source locations during the time-reversed simulations (Figures 10 and 11) and in every case except one, the initial moment tensor is found reasonably well. Before and after the increase in amplitudes in Figures 10 and 11, the stress is nearly zero which is also the case for points far away from the source location. In the cases with noise added to the displacement data, the stress traces are noisy as well (Figures 10c and 10e). For the case with the rudimentary one-dimensional model and no noise added to the displacement data, the stress traces appear noisy around the source origin time (Figure 10d). This noise is removed from the stress traces by additionally recording the stress at the source location in the non-time reversed simulation and muting amplitudes in the time-reversed stress traces smaller than the peak noise level found in the non-time-reversed stress traces. The resulting stress traces are comparable to the initial moment tensor (Figure 10a).

By picking the maxima in each stress trace, the scalar moment tensor is determined. Smoothing of the time-dependent moment tensor before picking the maxima was omitted since TRI is able to locate and characterize sources with a $SNR < 1$ and smoothing may amplify the noise rather than the signal. For the cases with the three-dimensional model (Figures 10b and 10c), the maxima occur simultaneously. This time is taken as the origin time and is correctly at 3 s in these cases (see Table 2). For the cases with the one-dimensional velocity model (Figures 10d and 10e), the individual maxima are slightly shifted in time due to inaccurate travel times between receivers and the source. However, if the time-shifted maxima are picked, the scalar moment tensor is comparable to the other cases. In this case, the origin time is taken as the time of the maximum with the highest amplitude in the stress traces and deviates a few timesteps from the true origin time. These post-processing steps of the stress traces are outlined in Figure 4c.

The derived scalar moment tensors are compared using the decomposition of the moment tensor proposed by Knopoff and Randall (1970), calculating the fault planes and plotting the focal mechanism solutions using the MoPad tool (Krieger and Heimann, 2012). A slight deviation from the initial moment tensor (Figure 10a) is observed for the case with the three-dimensional velocity model without noise (Figure 10b and Table 2). This is most likely due to the receivers being located only at the surface. The isotropic part seems not to be fully reconstructed when using only surface stations. However, the simple synthetic case with a homogeneous velocity model (Figure 3) shows that in principal a pure isotropic source can be reconstructed using only surface stations. Therefore, the irregular station distribution in combination with the correct but heterogeneous velocity model may hinder the correct reconstruction of the isotropic part of the source. The DC part of the source is determined correctly as can be seen by the focal mechanism solutions and the fault planes. In the case of two sources in the three-dimensional velocity model and without noise (Figure 11 and Tab. 2), the first source is determined very similar to the case with only one source. The moment tensor of the second source is also recovered well but with slight deviations from a pure DC source. This demonstrates the ability of the method to cope with events that are not optimally positioned in relation to the station network.

The cases with the three-dimensional velocity model and noisy data (Figure 10c) and the one-dimensional model without noise produce (Figure 10d) very similar moment tensors to the one with the three-dimensional velocity model without noise (Figure 10b). The case with the one-dimensional velocity model and noise (Figure 10e) produces very high noise levels in the traces which causes some moment tensor components to be zero. The scalar moment tensor for this case differs from that of the other cases. Since this case is the one where the source location uncertainty is high and would be categorized as unsuccessful, the conclusion is that in these synthetic cases moment tensors are correctly reconstructed if the source location can be distinguished unambiguously from artificial convergence locations.

LOCATING AND CHARACTERIZING SELECTED MICRO-EARTHQUAKES IN LOS HUMEROS

The derived workflow (Figure 4) is applied to field data recorded at the geothermal field of Los Humeros with three-component stations. There were ten short-period ('DS' in Figure

5) and 17 broadband stations ('DB' in Figure 5) distributed at the surface. Two prominent challenges arise with this field dataset: (1) The stations are positioned irregularly which results in source location inaccuracies as shown in Finger and Saenger (2020), and (2) the best-constrained velocity model at this time is a one-dimensional velocity model (Löer et al., 2020) which is used here in the same smoothed version as presented in Finger and Saenger (2020).

Locate and characterize micro-earthquakes with one-dimensional velocity model

To minimize challenges from low signal-to-noise ratios, of the micro-earthquakes reported in Jousset et al. (2019) three of the largest magnitude events are selected. The three-component velocity data are converted to displacement data, resampled to the used time increment in the FD simulation, filtered, and normalized.

The unprocessed traces reveal a frequency content roughly in the range of 1 Hz to 30 Hz. Therefore, two different frequency bands are used: 2Hz to 12 Hz and 1Hz to 30 Hz. The frequency band covers most of the frequency spectrum visible in the unprocessed data while the first frequency band only images the lower frequency part, excluding the very low frequencies to obtain a slightly narrower frequency band, and may enable better convergence with the used velocity model since no small-scale structures are resolved in the velocity model. The two different frequency bands require different model sizes and grid spacings to avoid numerical dispersion while keeping computational costs reasonable. For the smaller frequency band, the same model dimensions as for the realistic model are used (Figure 5). For the larger frequency band, the model size is reduced to -5 km to 5 km in x- and y-direction. The grid spacing is reduced to $\Delta x = 10\,\mathrm{m}$ and the time increment is reduced to $\Delta t = 0.0009\,\mathrm{s}$. The depth of the model is 6 km in both cases.

The vertical displacement filtered between $2-12\,\mathrm{Hz}$ is shown in Figure 12 for the three selected events. For two of the events, 22 stations and for the third event 20 of the stations were actively recording at the time of the event. For the smaller model, stations outside the model boundaries were not used which reduces the number of available stations.

The workflow in Figure 4a is followed to locate the events. Additionally, the sensitivity maps derived in Finger and Saenger (2020) are used to mute areas in the TRI image volumes where no source location is possible due to the station positions and the velocity model. The sensitivity map derived for strike-slip sources is used here and applied to all imaging conditions since a high DC content is expected. This sensitivity map can be seen as an estimate for the spatial variability of source-location accuracies for sources with a high shear-wave content. The smaller model for the larger frequency range covers the part with mostly very high source location accuracies in the sensitivity maps and thus no sensitivity map is used in this case. However, the top 500 m are muted since the stations are too far apart to locate sources in such shallow depths (Werner and Saenger, 2018) and thus artificial convergence locations are suppressed.

To distinguish artificial convergence locations from source locations, all convergence locations smaller than half the minimal S-wave wavelength, $\lambda_{\mathrm{S},min} = 216\,\mathrm{m}$ for the smaller frequency range or $\lambda_{\mathrm{S},min} = 86.5\,\mathrm{m}$ for the broader frequency range, are eliminated in all three imaging conditions. The remaining convergence locations are sorted by their relative amplitudes and the amplitudes and radii are plotted in Figure 13.

The amplitude decay for the $2-12\,\mathrm{Hz}$ filtered data (Figure 13a) appears similar as those for the rudimentary one-velocity model in the realistic scenario (Figure 9b). The amplitude drop is very small and thus source locations and artificial convergence locations cannot be distinguished. For the $1 - 30\,\mathrm{Hz}$ data, the amplitudes decay more rapidly. However, considerably less convergence locations are found than for the other cases and no plateau is reached for the amplitudes. Nevertheless, convergence locations are selected to determine the moment tensors. Since no other differentiation is possible, convergence locations larger than $1\,\lambda_{\mathrm{S},min}$ are assumed to present the best converged spots and are chosen for further investigations. The three largest-amplitude convergence locations for the event on 2018, April 22, obtained with the narrower frequency band and the second and fourth largest-amplitude convergence spot for the event on 2018, April 29, obtained with the narrower frequency band are chosen (larger green circles in Figure 13).

The three analysed convergence locations for the event on 2018, April 22, are close together (Figure 14). They are only $4-6\,\lambda_{\mathrm{S},min}$ apart and deviate about the same distance from the source location reported in Jousset et al. (2019), obtained by traveltime location with a ray-based method. This indicates that the convergence locations are connected. The first and second convergence spot occur at the same time and have very similar fault plane solutions (Table 3). However, the first convergence spot has a larger DC content while the second convergence spot has a very high CLVD content. The third convergence spot occurs about $0.5\,\mathrm{s}$ later than the first two and is located shallower. However, it occurred at the exact east coordinate of the first convergence spot. The fault plane solution is almost a pure strike-slip solution. A possible explanation may be that this convergence spot images a secondary event triggered by the first one. However, since only a one-dimensional velocity model is used, the source image could significantly change when using a three-dimensional velocity model thus indicating that the convergence locations results from an incomplete interference of the wavefield.

The two convergence locations analysed for the event on 2018, April 29, are nearly 3 km apart and are thus interpreted as two events or one event and one artefact (Figure 15). The convergence spot number four (Figure 15b) is only about $2.5\,\lambda_{\mathrm{S},min}$ away from the source location reported in Jousset et al. (2019) for this event. The fault plane solutions presented in Figure 15 and Table. 3 are very similar to those obtained using first motions of P-wave arrivals (Jousset et al. (2019)). We are confident that this convergence spot number four is the same one reported in Jousset et al. (2019). However, the convergence spot number two has a higher relative amplitude and a similar radius (Figure 13). It occurred slightly more than a second before the other event. It is possible that this event has been missed by the analysis reported in Jousset et al. (2019) due to its overlap in the recorded traces. Nevertheless, it cannot be excluded that this is an artefact. A better-constrained velocity model may allow to confirm or contradict that this event is in fact two events.

DISCUSSION

Synthetic tests revealed that the recorded stress tensor may be used to determine the time-dependent moment tensor. In most cases, the initial moment tensor could be reconstructed correctly when the noise was removed from the stress traces and the time-shifted local maxima were picked as the moment tensor components. By using the noise level obtained in the non-time-reversed simulation to remove noise from the stress traces of the time-reversed simulation and picking (time-shifted) local maxima in the stress traces, a reliable way is found to recover the scalar moment tensor correctly. However, small amplitude parts of the seismic wavelet, that are indistinguishable from the noise, are suppressed by this method as well. The recovered source wavelet may not be complete. For this noisesuppression method, it is assumed that the noise in the stress traces stems from the model setup and signals exceeding the determined background noise level are related to the source signal. Noisy displacement traces seem to result in predominantly noisy stress traces while a rudimentary velocity model causes noisy stress traces, time-shifted local maxima and errors in the origin time. The influence of the incorrect velocity model seems to be higher than the influence of low signal-to-noise ratios on the characterisation. If the velocity model is more accurate for P or S waves, a decoupling of the two may be possible which leads to an enlarged convergence location or two convergence locations. When the signal-to-noise ratio is low and simultaneously the velocity model is not completely correct, the moment tensor could not be recovered correctly, which is a similar behaviour as observed by other studies for the localisation of events (Werner and Saenger, 2018). Furthermore, effects like absorption or velocity anisotropies are not accounted for and are expected to add additional uncertainties in the source images.

Since the moment tensor may be determined for any convergence location, it is crucial to distinguish source locations from artificial convergence locations. The size of the convergence locations and the amplitude drop seem to be stable criteria for distinguishing between artificial convergence locations and source locations. Furthermore, the visual inspection of TRI image volumes supports the distinction.

Although synthetic tests were successful, the location and characterisation of microearthquakes in Los Humeros using TRI proves to be challenging. However, by strictly applying the derived workflow, two of the three selected events could be located and characterized although only a one-dimensional velocity model is currently available. The used velocity model does not accurately represent the heterogeneous subsurface and thus part of the wavefield that is not accounted for in the velocity model alters the wavefield at the source location. At the point of this study, no well-constrained three-dimensional velocity model has been derived from the passive seismic dataset (Toledo et al., 2019). The ambiguity of the source locations and the high level of noise in the stress traces support that the velocity model is not adequate. Furthermore, the velocity model does not depict small-scale heterogeneities. Therefore, the higher frequency part of the wavefield cannot be back propagated correctly and hinders focusing on the source location. Simulations that include the higher frequencies did not result in the location of sources. Although a realistic three-dimensional velocity model is derived using geologic information and used for the synthetic cases, it is too poorly constrained to be suitable for locating the events.

Selecting micro-earthquakes that were already located with a ray-based method (Jousset et al., 2019) ensured that the events were in a part of the model where the source location accuracy was adequate and most of the stations were actively recording. However, the synthetic tests imply that an irregular surface seismic network introduces errors in the moment-tensor determination. Additionally, the average altitude of the seismic stations is used as the surface of the model which is then planar and even. No topography was considered. Since the maximal height difference is about $340\,\mathrm{m} \approx 1.5\lambda_{\mathrm{S},min}$, the expected influence is neglectable.

The pre-processing of the recorded seismic traces was kept to a minimum so as not to assume anything about the sources. No site effects were included and the horizontal components were not rotated to align with the coordinate system since the needed rotation is small. Since only a one-dimensional velocity model is used here, there is no conflict between the velocity model and the alignment of the horizontal components. However, determined source locations may be slightly erroneous.

Since the number of events is not known or assumed before the beginning of the analysis, one challenge is to determine the number of events during the analysis of the TRI image volumes. This makes the distinction between artificial convergence locations and source locations challenging. The selected earthquakes were identified by a ray-based approach to be only a single event (Jousset et al., 2019). However, in this study, multiple locations were obtained for the two events that were analysed in detail. Future studies using a three-dimensional velocity model may reveal the true number of sources.

While in general TRI does not assume sources to be point sources, in the analysis of the image volumes it is assumed that the events are point sources. Manual inspection of the TRI image volumes may provide a more detailed understanding of the extent and shape of the converged energy at the source location. In this study, the focus was to provide source information as source location, moment tensor and origin time.

The determination of the scalar moment tensor from the time-dependent moment tensor is more challenging in the field data case than in the synthetic cases. After the noise level is eliminated, a time window has to be chosen in which to pick the local maxima of the stress traces. As the synthetic tests suggest, a time shift is expected if the velocity model is incorrect. However, the time window in which to pick local maxima has to be limited around the determined origin time in order to be certain to pick a value that is associated with the source. The scalar moment tensor is highly sensitive to the chosen time window as larger time windows may include signals from other sources that inhibit the correct determination of the moment tensor.

For two of the three selected earthquakes, source locations and moment tensor could be determined and roughly fit the results of the ray-based method as reported in Jousset et al.

(2019). Therefore, the proposed workflow provides a first estimate of the source location and the time-dependent moment tensor for this application test, which can be improved with an updated velocity model. However, the comparison of results from ray-based methods and TRI should be done carefully. Ray-based methods use the arrival time of the seismic phases to locate the events and most likely locate the beginning of the possible rupture, i.e. the point where the first energy was released. TRI locates the point where the highest level of energy was released. Depending on the rupture size and source mechanism, these points do not necessarily coincide, especially for larger-magnitude events. Furthermore, in ray-based methods, the traces are filtered in a certain range before picking the phases. If the frequency range is not the same as for TRI, location and especially characterisation results will differ. In general, methods based on wave equation solutions can handle strong velocity contrasts and are therefore advantageuous over ray-based methods. Lastly, the same velocity model should be used for both methods.

CONCLUSION

A workflow was derived to locate and characterize seismic events using TRI. It was found that the total energy density imaging condition $\mathbf{I}_{\mathrm{e}}$ correctly recovers the source location while the S-wave energy density imaging condition $\mathbf{I}_{\mathrm{S}}$ and the P-wave energy density $\mathbf{I}_{\mathrm{P}}$ image the source radiation pattern and may be zero at the source location. The time-dependent moment tensor has been derived by recording the stress traces at determined source locations during the back propagation of the time-reversed wave field. By defining that convergence spot radii should be at least $0.5\lambda_{\mathrm{S},min}$ and comparing the relative amplitudes of convergence locations, robust criteria were derived for distinguishing artificial convergence locations from source locations. If these criteria are met by a source location, the determined time-dependent moment tensor represents the initial moment tensor closely in the synthetic cases. Furthermore, the TRI image volumes may be inspected to further evaluate the quality of the source location. Synthetic tests revealed that although low signal-to-noise ratios and irregular station distribution influence the location and characterisation accuracy, the influence of a rudimentary one-dimensional velocity model has the most detrimental effect. Nevertheless, selected micro-seismic events in Los Humeros, Mexico, could be located and characterized with the used one-dimensional velocity model. These results need to be refined once a well-constrained three-dimensional velocity model has been derived.

ACKNOWLEDGMENTS

The authors would like to acknowledge the Comisión Federal de Electricidad (CFE) for kindly providing support and advice and for granting access to their geothermal fields for the deployment of the seismic stations. We also acknowledge our Mexican and European colleagues for their help and collaboration in deployment, maintenance and retrieval of the stations. This project received funding from the European Union's Horizon 2020 research and innovation programme under grant agreement no. 727550 (http://www.gemex-h2020.eu, last access: 9th December 2020).

REFERENCES

Aki, K. and P. Richards, 1980, Quantitative Seismology: Theory and Methods: WH Freeman & Co.

Albaric, J., V. Oye, N. Langet, M. Hasting, I. Lecomte, K. Iranpour, M. Messeiller, and P. Reid, 2014, Monitoring of induced seismicity during the first geothermal reservoir stimulation at Paralana, Australia: Geothermics, **52**, 120–131.

Artman, B., I. Podladtchikov, and B. Witten, 2010, Source location using time-reverse imaging: Geophysical Prospecting, **58**, 861–873.

Calcagno, P., G. Evanno, E. Trumpy, L. C. Gutiérrez-negrín, J. L. Macías, G. Carrasco-núñez, and D. Liotta, 2018, Preliminary 3-D geological models of Los Humeros and Acoculco geothermal fields (Mexico) – H2020 GEMex Project: Advances in Geosciences, 321–333.

Cesca, S., A. Rohr, and T. Dahm, 2013, Discrimination of induced seismicity by full moment tensor inversion and decomposition: Journal of Seismology, **17**, 147–163.

Chambers, K., B. D. Dando, G. A. Jones, R. Velasco, and S. A. Wilson, 2014, Moment tensor migration imaging: Geophysical Prospecting, **62**, 879–896.

Clayton, R. W. and B. Engquist, 1980, Absorbing boundary conditions for wave-equation migration: Geophysics, **45**, 895–904.

Deichmann, N. and D. Giardini, 2009, Earthquakes Induced by the stimulation of an enhanced geothermal system below Basel (Switzerland): Seismological Research Letters, **80**, 784–798.

Ellsworth, W. L., D. Giardini, J. Townend, S. Ge, and T. Shimamoto, 2019, Triggering of the Pohang, Korea, Earthquake (Mw 5.5) by enhanced geothermal system stimulation: Seismological Research Letters, **90**, 1844–1858.

Finger, C. and E. H. Saenger, 2020, Sensitivity Maps for Time-Reverse Imaging: An Accuracy Study for the Los Humeros Geothermal Field (Mexico): Geophysical Journal International, **222**, 231–246.

Fink, M., D. Cassereau, A. Derode, C. Prada, P. Roux, M. Tanter, J.-L. Thomas, and F. Wu, 1999, Time-reversed acoustics: Reports on progress in Physics, **281**, 91–97.

Franczyk, A., 2019, Using the Morris sensitivity analysis method to assess the importance of input variables on time - reversal imaging of seismic sources: Acta Geophysica, **67**, 1525–1533.

Gajewski, D. and E. Tessmer, 2005, Reverse modelling for seismic event characterization: Geophysical Journal International, **163**, 276–284.

Gaucher, E., M. Schoenball, O. Heidbach, A. Zang, P. A. Fokker, J. D. Van Wees, and T. Kohl, 2015, Induced seismicity in geothermal reservoirs: A review of forecasting approaches: Renewable and Sustainable Energy Reviews, **52**, 1473–1490.

Gephart, J. W. and D. W. Forsyth, 1984, An improved method for determining the regional stress tensor using earthquake focal mechanism data: application to the San Fernando earthquake sequence.: Journal of Geophysical Research, **89**, 9305–9320.

Gharti, H. N., V. Oye, D. Kühn, and P. Zhao, 2011, Simultaneous microearthquake location and moment-tensor estimation using time-reversal imaging: SEG Technical Program Expanded Abstracts 2011, 1632–1637.

Hardt, M. and F. Scherbaum, 1994, The design of optimum networks for aftershock recordings: Geophysical Journal International, **117**, 716–726.

Häring, M. O., U. Schanz, F. Ladner, and B. C. Dyer, 2008, Characterisation of the Basel 1 enhanced geothermal system: Geothermics, **37**, 469–495.

Jolie, E., D. Bruhn, A. L. Hernández, D. Liotta, V. H. Garduño-monroy, M. Lelli, G. P.

Hersir, C. Arango-galván, D. Bonté, P. Calcagno, P. Deb, C. Clauser, A. F. H. Ochoa, E. Huenges, Z. Ivonne, G. Acevedo, K. Kieling, E. Trumpy, J. Vargas, L. C. Gutiérrez-negrín, A. Aragón-aguilar, S. Halldórsdóttir, and E. G. Partida, 2018, GEMex – A Mexican-European Research Cooperation on Development of Superhot and Engineered Geothermal Systems: Proceedings on the 43rd Workshop on Geothermal Reservoir Engineering, 1–10.

Jousset, P., K. Asgustsson, E. Barison, G. Böhm, M. Calò, I. Chavarria, B. Farina, E. Gaucher, K. Löer, J. Martins, M. Perton, F. Poletto, E. H. Saenger, A. Soto, T. Toledo, A. Verdel, and C. Werner, 2019, Seismic structures of the Acoculco and Los Humeros geothermal fields (Deliverable 5.3 of Horizon2020 Project GeMex): Technical report.

Kawakatsu, H. and J. P. Montagner, 2008, Time-reversal seismic-source imaging and moment-tensor inversion: Geophysical Journal International, **175**, 686–688.

Kim, Y., Q. Liu, and J. Tromp, 2011, Adjoint centroid-moment tensor inversions: Geophysical Journal International, **186**, 264–278.

Knopoff, L. and M. J. Randall, 1970, The Compensated Linear-Vector Dipole: A possible Mechanism for Deep Earthquakes: Journal of Geophysical Research, **75**, 4957–4963.

Kocur, G. K., E. H. Saenger, C. U. Grosse, and T. Vogel, 2016, Time reverse modeling of acoustic emissions in a reinforced concrete beam: Ultrasonics, **65**, 96–104.

Köhn, D., D. De Nil, S. A. al Hagrey, and W. Rabbel, 2016, A combination of waveform inversion and reverse-time modelling for microseismic event characterization in complex salt structures: Environmental Earth Sciences, **75**, 1235.

Kremers, S., A. Fichtner, G. B. Brietzke, H. Igel, C. Larmat, L. Huang, and M. Käser, 2011, Exploring the potentials and limitations of the time-reversal imaging of finite seismic sources: Solid Earth, **2**, 95–105.

Krieger, L. and S. Heimann, 2012, MoPaD-Moment tensor plotting and decomposition:

A tool for graphical and numerical analysis of seismic moment tensors: Seismological Research Letters, **83**, 589–595.

Li, L., J. Tan, B. Schwarz, F. Staněk, N. Poiata, P. Shi, L. Diekmann, L. Eisner, and D. Gajewski, 2020, Recent Advances and Challenges of Waveform-Based Seismic Location Methods at Multiple Scales: Reviews of Geophysics, **58**, e2019RG000667.

Löer, K., T. Toledo, G. Norini, X. Zhang, A. Curtis, and E. H. Saenger, 2020, Imaging the deep structures of los humeros geothermal field, Mexico, using three-component seismic noise beamforming: Seismological Research Letters, **91**, 3269–3277.

Lokmer, I., G. S. O'Brien, D. Stich, and C. J. Bean, 2009, Time reversal imaging of synthetic volcanic tremor sources: Geophysical Research Letters, **36**, 1–6.

Lowrie, W., 2007, Fundamentals of Geophysics, second ed.: Cambridge University Press.

Maurer, V., E. Gaucher, M. Grunberg, R. Koepke, R. Pestourie, and N. Cuenot, 2020, Seismicity induced during the development of the Rittershoffen geothermal field, France: Geothermal Energy, **8**, 5.

Nakata, N. and G. C. Beroza, 2016, Reverse time migration for microseismic sources using the geometric mean as an imaging condition: Geophysics, **81**.

Norini, G., G. Carrasco-Núñez, F. Corbo-Camargo, J. Lermo, J. Hernández Rojas, C. Castro, M. Bonini, D. Montanari, G. Corti, G. Moratti, L. Piccardi, G. Chavez, M. C. Zuluaga, M. Ramirez, and F. Cedillo, 2019, The structural architecture of the Los Humeros volcanic complex and geothermal field: Journal of Volcanology and Geothermal Research.

Saenger, E. H., 2011, Time reverse characterization of sources in heterogeneous media: NDT and E International, **44**, 751–759.

Saenger, E. H., N. Gold, and S. A. Shapiro, 2000, Modeling the propagation of elastic waves using a modified finite-difference grid: Wave Motion, **31**, 77–92.

Schoenball, M., N. C. Davatzes, and J. M. Glen, 2015, Differentiating induced and natural seismicity using space-time-magnitude statistics applied to the Coso Geothermal field: Geophysical Research Letters, **42**, 6221–6228.

Shapiro, S. A., E. Rothert, V. Rath, and J. Rindschwentner, 2002, Characterization of fluid transport properties of reservoirs using induced microseismicity: Geophysics, **67**, 212–220.

Steiner, B., E. H. Saenger, and S. M. Schmalholz, 2011, Time-reverse imaging with limited S-wave velocity model information: Geophysics, **76**, MA33–MA40.

Toledo, T., E. Gaucher, M. Malte, M. Calò, A. Figueroa, P. Jousset, K. Kieling, and E. Saenger, 2019, Dataset of the 6G seismic network at Los Humeros, 2017-2018: GFZ Data Services.

Werner, C. and E. H. Saenger, 2018, Obtaining reliable source locations with time reverse imaging: Limits to array design, velocity models and signal-to-noise ratios: Solid Earth, **9**, 1487–1505.

Willacy, C., E. Van Dedem, S. Minisini, J. Li, J. W. Blokland, I. Das, and A. Droujinine, 2019, Full-waveform event location and moment tensor inversion for induced seismicity: Geophysics, **84**, KS39–KS57.

Witten, B. and B. Artman, 2011, Signal-to-noise estimates of time-reverse images: Geophysics, **76**, MA1–MA10.

Witten, B. and J. Shragge, 2017, Image-domain velocity inversion and event location for microseismic monitoring: Geophysics, **82**, KS71–KS83.

Zhao, L., P. Chen, and T. H. Jordan, 2006, Strain Green's tensors, reciprocity, and their applications to seismic source and structure studies: Bulletin of the Seismological Society of America, **96**, 1753–1763.

Zhao, M., Y. Capdeville, and H. Zhang, 2016, Direct numerical modeling of time-reversal acoustic subwavelength focusing: Wave Motion, **67**, 102–115.

LIST OF TABLES

LIST OF FIGURES

artificial spots and source locations and c) determining the moment tensor.

5 Locations of 27 stations of the temporary passive seismic network (Toledo et al., 2019) deployed at the geothermal field of Los Humeros. The mean station spacing is 1.5 km. The epicenter locations of the synthetic sources are marked with red stars. The origin of the model is at $19°40.2'$ N and $-97°27'$ W. The inset map shows the study area on the North American Continent. A description of the geology may be found in Norini et al. (2019).

6 Vertical profiles extracted from the three-dimensional realistic model generated by extrapolating the geologic interpretation in Norini et al. (2019) and the seismic velocities given for the geologic horizons in Löer et al. (2020). Left column shows P-wave velocities and right column shows S-wave velocities. a) - f) are slices in east-direction and g) - l) are slices in north direction. The first synthetic source position is marked in the responding slices with red stars and the approximated receiver aperture is marked with a blue double arrow.

7 a) Vertical component of pre-processed time-reversed displacement traces recorded at the 27 stations during the forward simulation with the single synthetic source. b) Vertical component of pre-processed time-reversed displacement traces for the forward simulation with two synthetic sources. c) Displacement traces in a) with additional white noise so that the signal-to-noise ratio is approximately 1.

8 Slices of TRI image volumes, zoomed on source locations, produced with $\mathbf{I}_\mathrm{e}$ at the initial source positions. a) - d) are for the cases with a single synthetic source. e) and f) show the case with the two sources. Slices are at the east location of the respective source (-1.38 km and 2.4 km).

9 Characteristics of convergence locations for different synthetic test cases in a realistic scenario with one or two sources. a) Deviations of convergence locations to true source

location with highest amplitudes for individual imaging conditions, given in multiples of $\lambda_{s,min} = 221.57\,\mathrm{m}$. b) Relative amplitudes and c) radii of the 10 highest-amplitude convergence locations in $\mathbf{I}_{\mathrm{e}}$. In b) and c) the first convergence spot relates to the source location and the location plotted in a).

10 a) Initial moment tensor. b) to e) stress recorded at source location during reverse simulation for varying cases. The origin time is marked by a vertical red line. The noise level determined from the illumination map simulation is marked as a grey bar in the left plots for each case. In the right plots for each case, the time-dependent moment tensor is shown zoomed in and with supppressed noise. Focal Mechanism solutions were produced with the double-couple part of the obtained scalar moment tensor and using the code provided by Krieger and Heimann (2012).

11 Characterization result for two synthetic sources with the three-dimensional model and without noise added to the displacement data. The origin time is marked by a vertical red line. The peak noise level of the stress traces is determined from the illumination map simulation and is marked as a grey bar in the left plots for each case. In the right plots for each case, the time-dependent moment tensor is shown zoomed in and with supppressed noise. Focal Mechanism solutions were produced with the double-couple part of the obtained scalar moment tensor and using the code provided by Krieger and Heimann (2012)

12 Vertical component of pre-processed (filtered between 2 Hz and 12 hz) and time-reversed displacement data from all available stations. a) Event recorded on 2018, April 22, b) event recorded on 2018, April 29 and c) event recorded on 2017, October 11.

13 Characteristics of convergence locations for different microseismic events in two frequency bands. a) Amplitudes and b) radii of the 15 highest-amplitude convergence locations in $\mathbf{I}_{\mathrm{e}}$. Green circles mark convergence locations selected for analysis. Spots with a

radius larger than $1\,\lambda_{\mathrm{S},min}$ were selected although the amplitude distribution did show as significant amplitude drops as in Figure 9.

14 Location and characterisation results for the event on 2018, April 22. Convergence locations in $\mathbf{I}_{\mathrm{e}}$ with a radius larger than $1\lambda_{\mathrm{S},min}$ are compared.

15 Location and characterisation results for the event on 2018, April 29. Convergence locations in I_e with a radius larger than $1\lambda_{\mathrm{S},min}$ are compared.

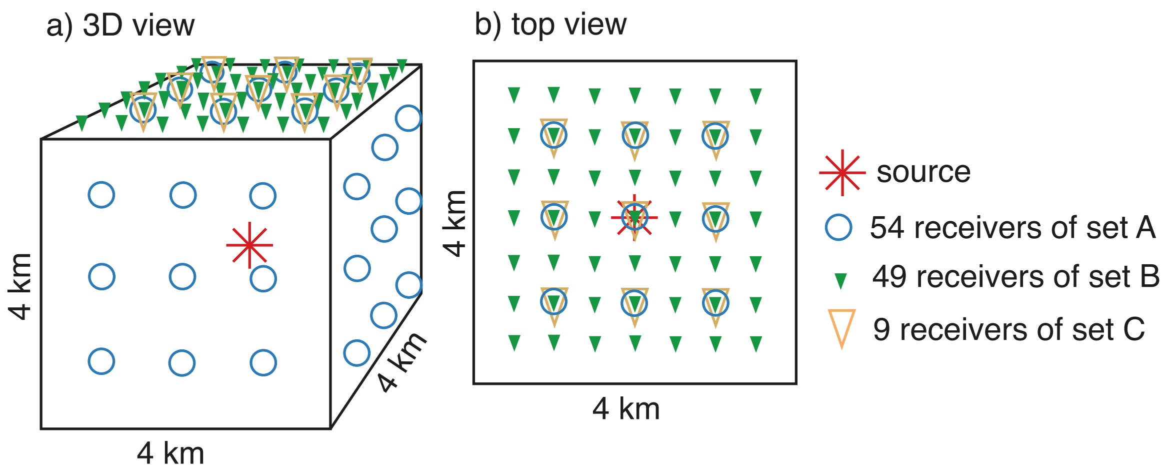

Figure 1: Set-up for the synthetic cube model. The source is located in the center of the cube. Three receiver sets are used: Set A with 54 receivers with nine receivers evenly distributed on each of the six sides of the cube, Set B with 49 receivers evenly distributed at the top side of the cube and Set C with nine receivers evenly distributed at the top side of the cube. a) Shows a three-dimensional view of the cube and b) shows only the top side.

Finger & Saenger – GEO-2020-0348

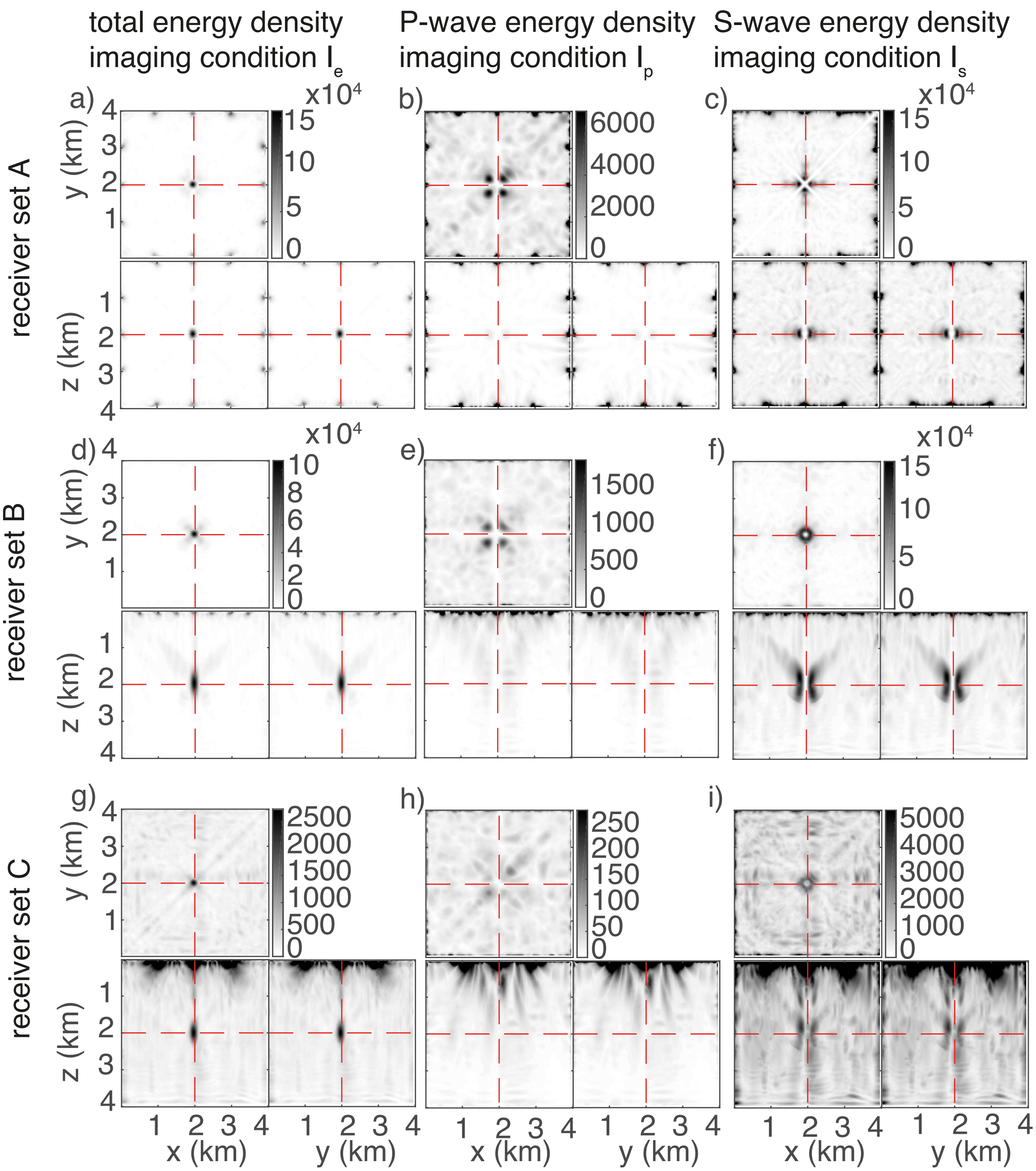

Figure 2: TRI image volumes for synthetic strike-slip source (only $M_{xy} \neq 0$) in a homogeneous cube model. Red dashed lines mark source positions in all slices. $\mathbf{I}_\mathrm{e}$, $\mathbf{I}_\mathrm{p}$ and $\mathbf{I}_\mathrm{S}$ are shown for selected slices at the initial source position. a) to c) are the results using receiver set A, d) to f) use receiver set B and g) to i) use receiver set C. Colormap shows amplitudes of the imaging conditions.

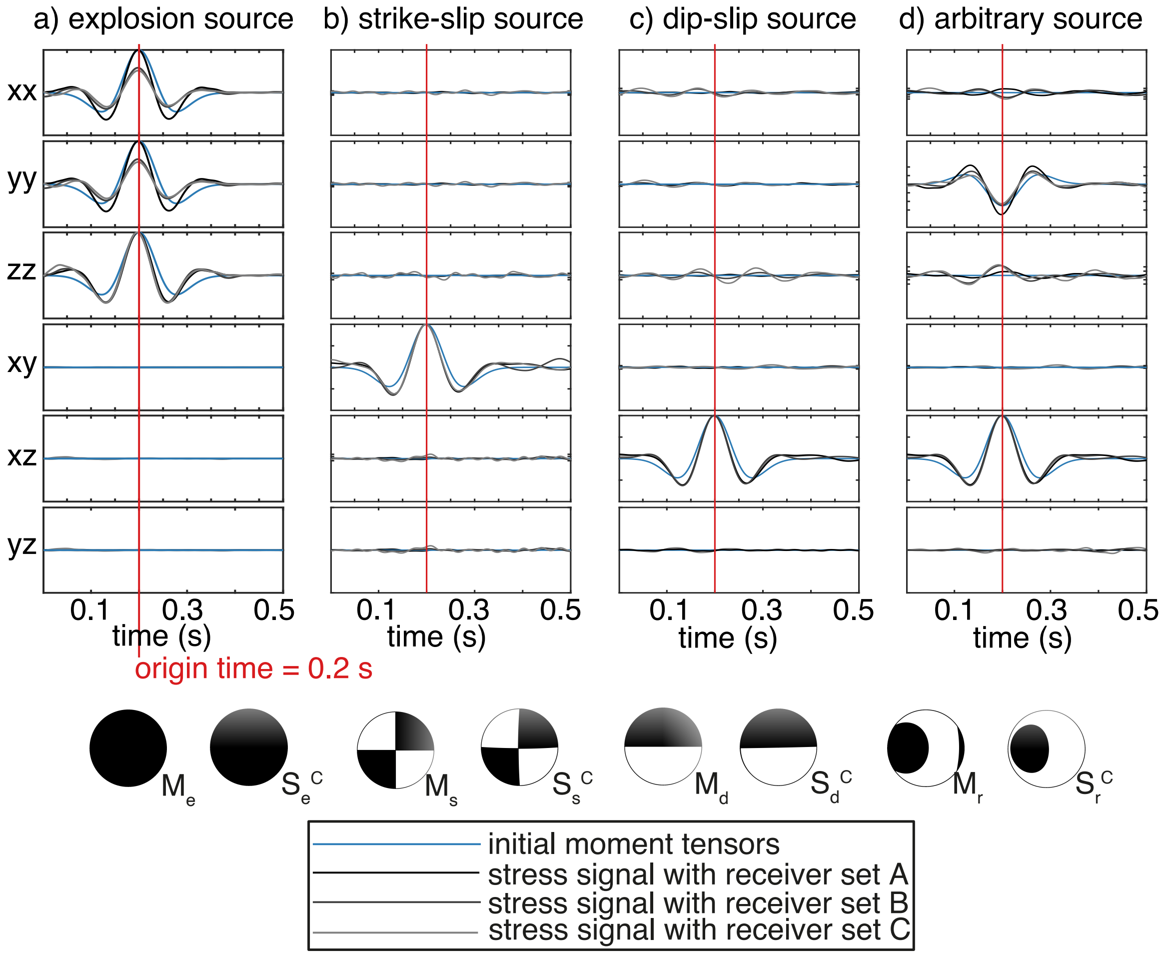

Figure 3: Initial time-dependent moment tensor M and stress tensor with receiver set A (S^A), receiver set B (S^B) and receiver set C (S^C) for the four tested synthetic source types. For the stress signals, the time axis is inverted to compensate for the time-reversed simulation. The amplitudes are scaled to minus one to plus one. The initial origin time is marked with a vertical red line. Focal mechanism plots are shown for the initial moment tensors and the moment tensors determined using stress traces recorded while using receiver set C. The full moment tensor is used for plotting the focal mechanism solution for the explosion and arbitrary source type, the double-couple part of the moment tensor is used for plotting the strike-slip and dip-slip source types. Focal Mechanism plots were created with the MoPad tool (Krieger and Heimann, 2012)

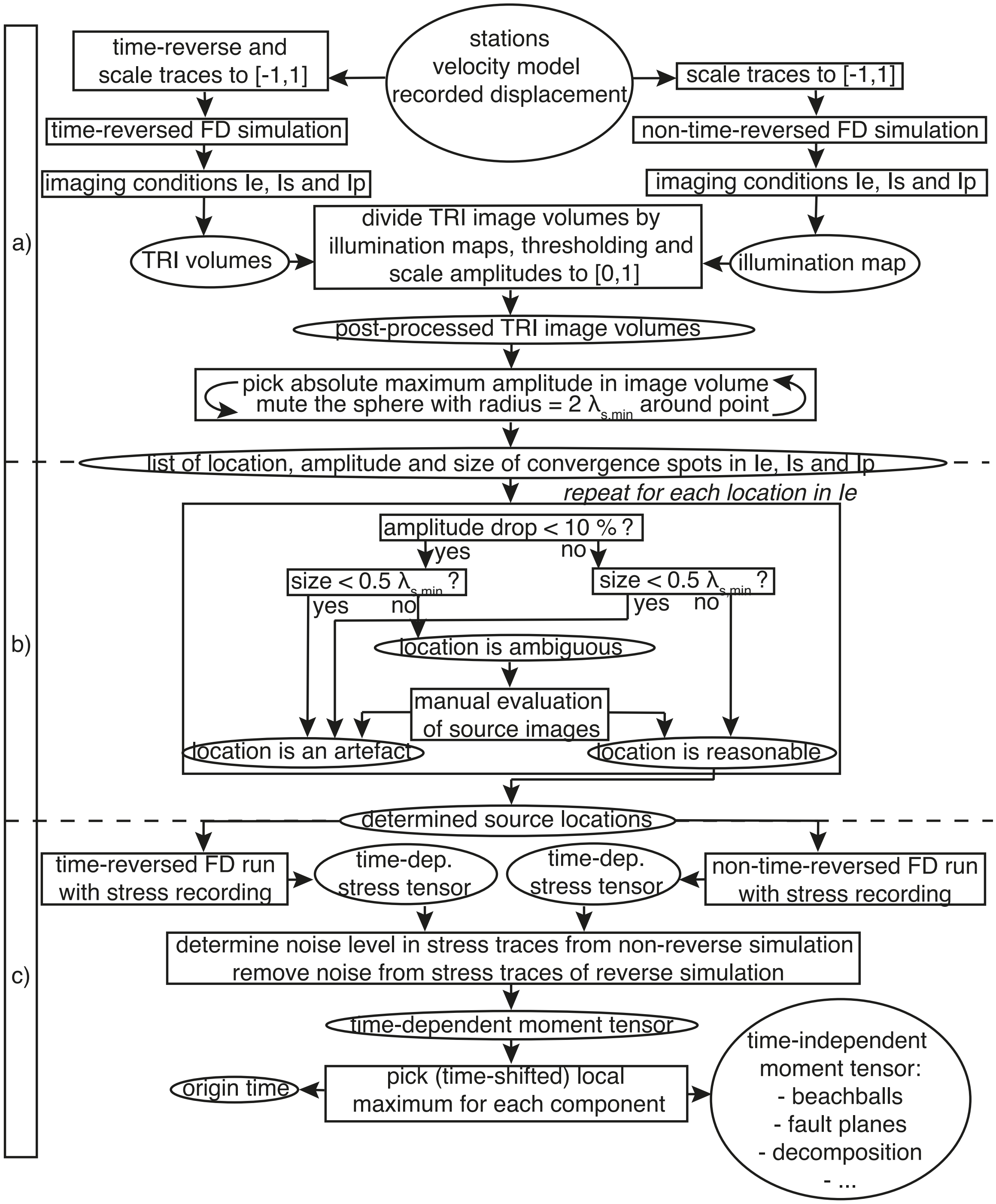

Figure 4: Workflow derived for locating and characterising seismic events with TRI. The workflow is separated into three parts: a) Obtaining the location and properties of the convergence locations, b) determining the quality of the convergence and sorting them into artificial spots and source locations and c) determining the moment tensor.

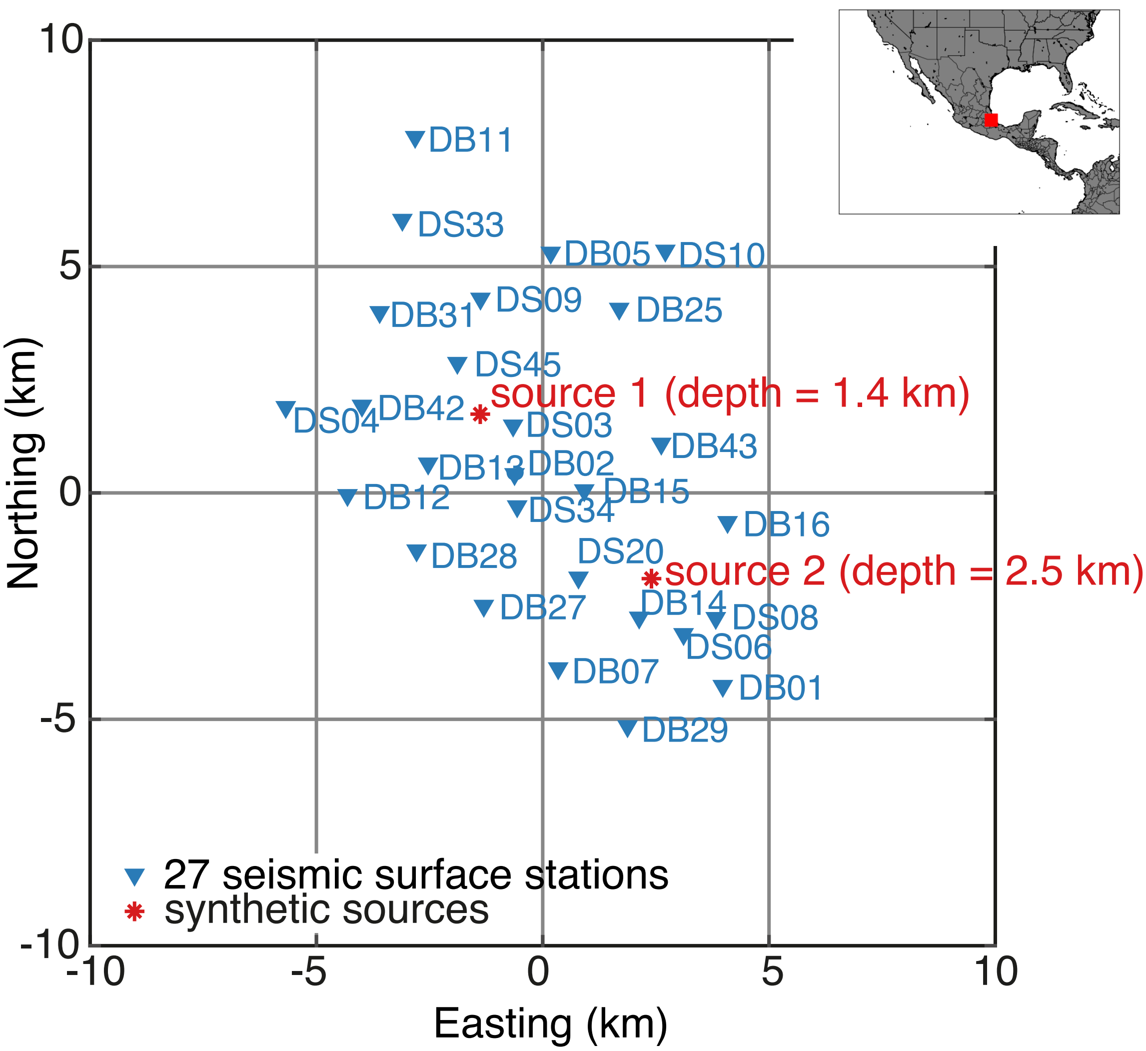

Figure 5: Locations of 27 stations of the temporary passive seismic network (Toledo et al., 2019) deployed at the geothermal field of Los Humeros. The mean station spacing is 1.5 km. The epicenter locations of the synthetic sources are marked with red stars. The origin of the model is at 19°40.2′ N and −97°27′ W. The inset map shows the study area on the North American Continent. A description of the geology may be found in Norini et al. (2019).

Finger & Saenger – GEO-2020-0348

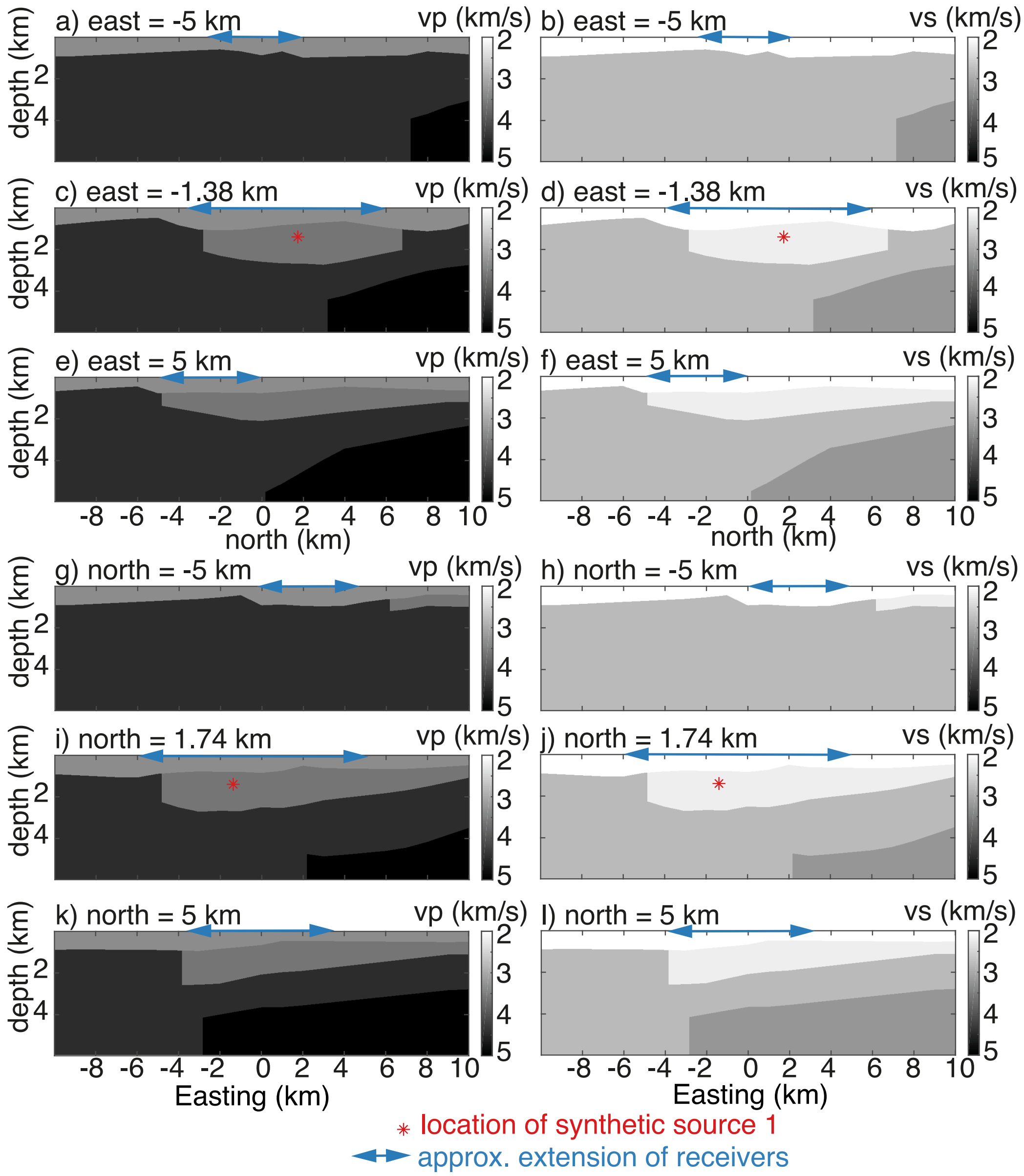

Figure 6: Vertical profiles extracted from the three-dimensional realistic model generated by extrapolating the geologic interpretation in Norini et al. (2019) and the seismic velocities given for the geologic horizons in Löer et al. (2020). Left column shows P-wave velocities and right column shows S-wave velocities. a) - f) are slices in east-direction and g) - l) are slices in north direction. The first synthetic source position is marked in the responding slices with red stars and the approximated receiver aperture is marked with a blue double arrow.

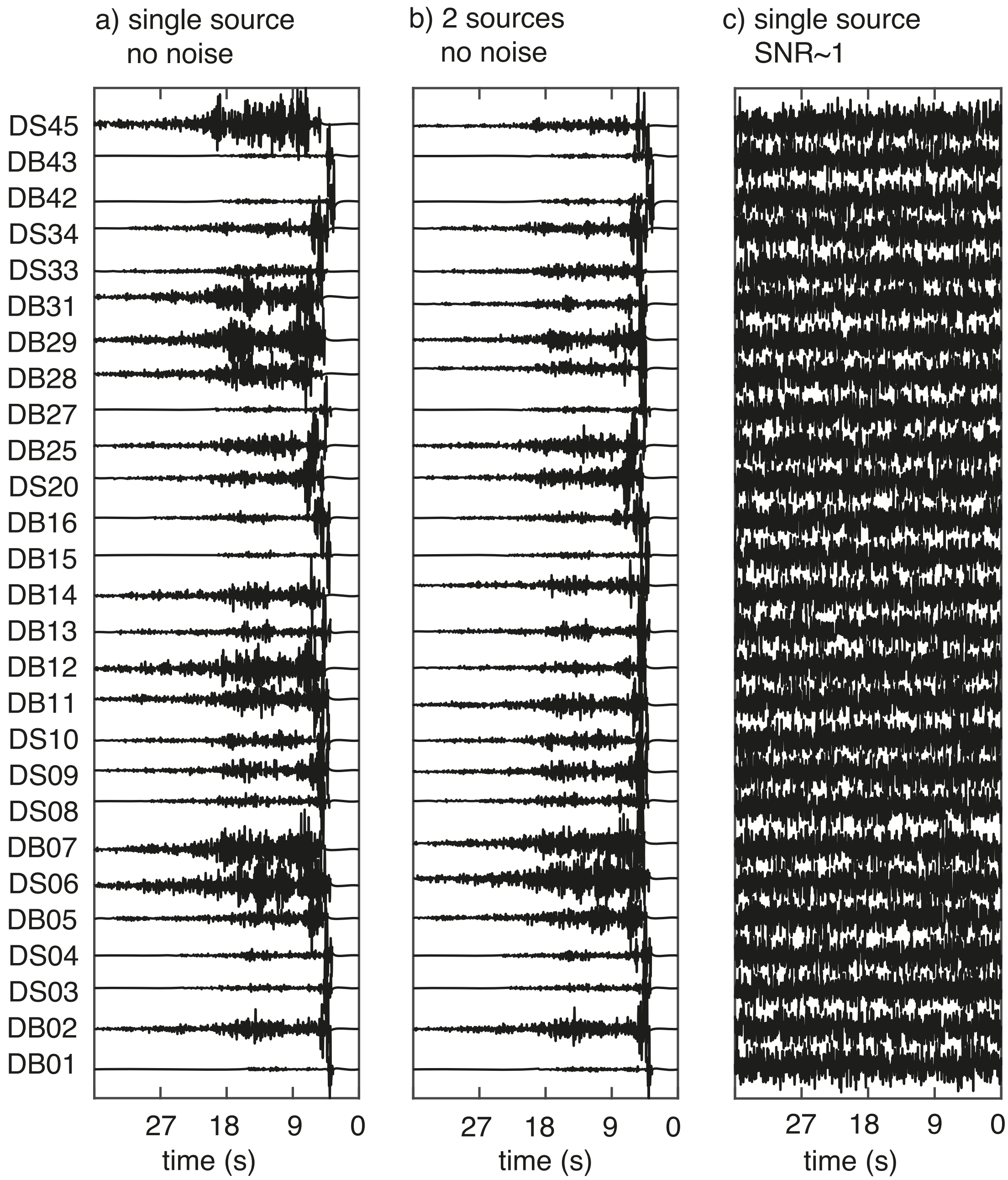

Figure 7: a) Vertical component of pre-processed time-reversed displacement traces recorded at the 27 stations during the forward simulation with the single synthetic source. b) Vertical component of pre-processed time-reversed displacement traces for the forward simulation with two synthetic sources. c) Displacement traces in a) with additional white noise so that the signal-to-noise ratio is approximately 1.

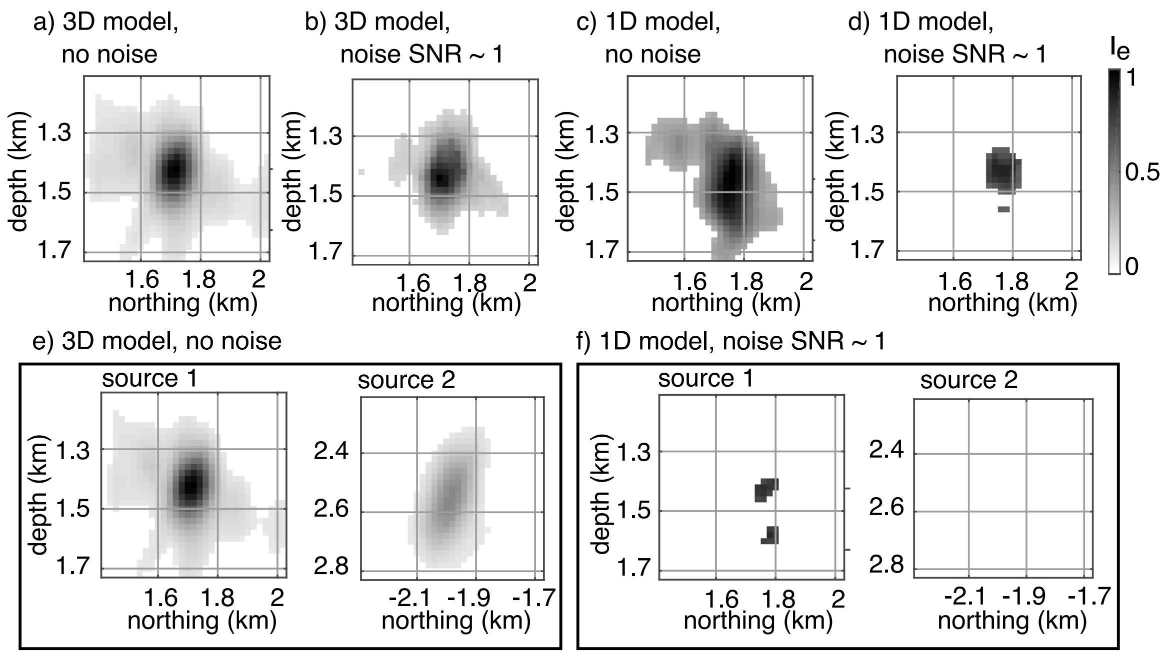

Figure 8: Slices of TRI image volumes, zoomed on source locations, produced with $\mathbf{I}_{\mathrm{e}}$ at the initial source positions. a) - d) are for the cases with a single synthetic source. e) and f) show the case with the two sources. Slices are at the east location of the respective source (-1.38 km and 2.4 km).

Finger & Saenger – GEO-2020-0348

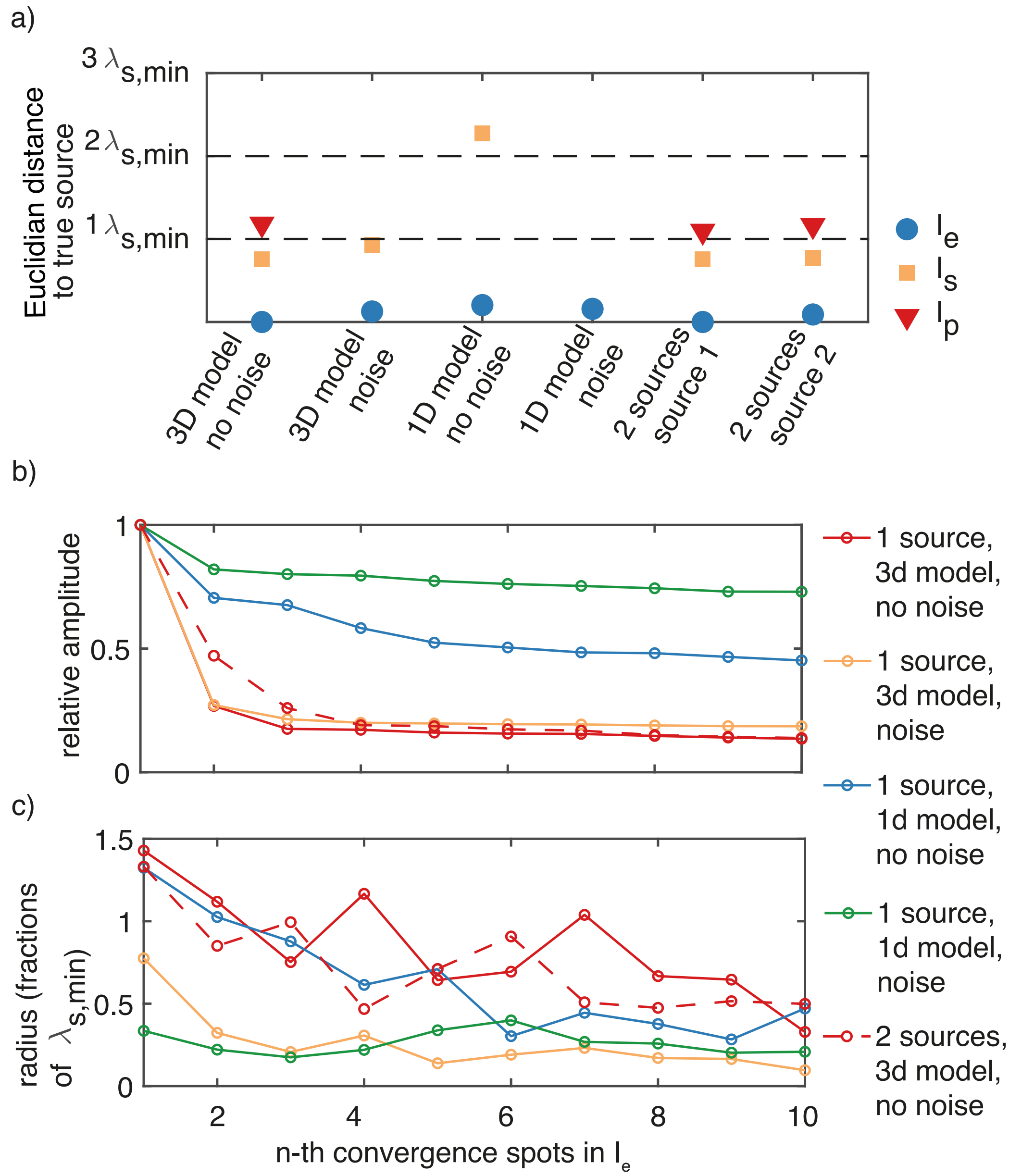

Figure 9: Characteristics of convergence locations for different synthetic test cases in a realistic scenario with one or two sources. a) Deviations of convergence locations to true source location with highest amplitudes for individual imaging conditions, given in multiples of $\lambda_{s,min} = 221.57\,\mathrm{m}$. b) Relative amplitudes and c) radii of the 10 highest-amplitude convergence locations in $\mathbf{I}_\mathrm{e}$. In b) and c) the first convergence spot relates to the source location and the location plotted in a).

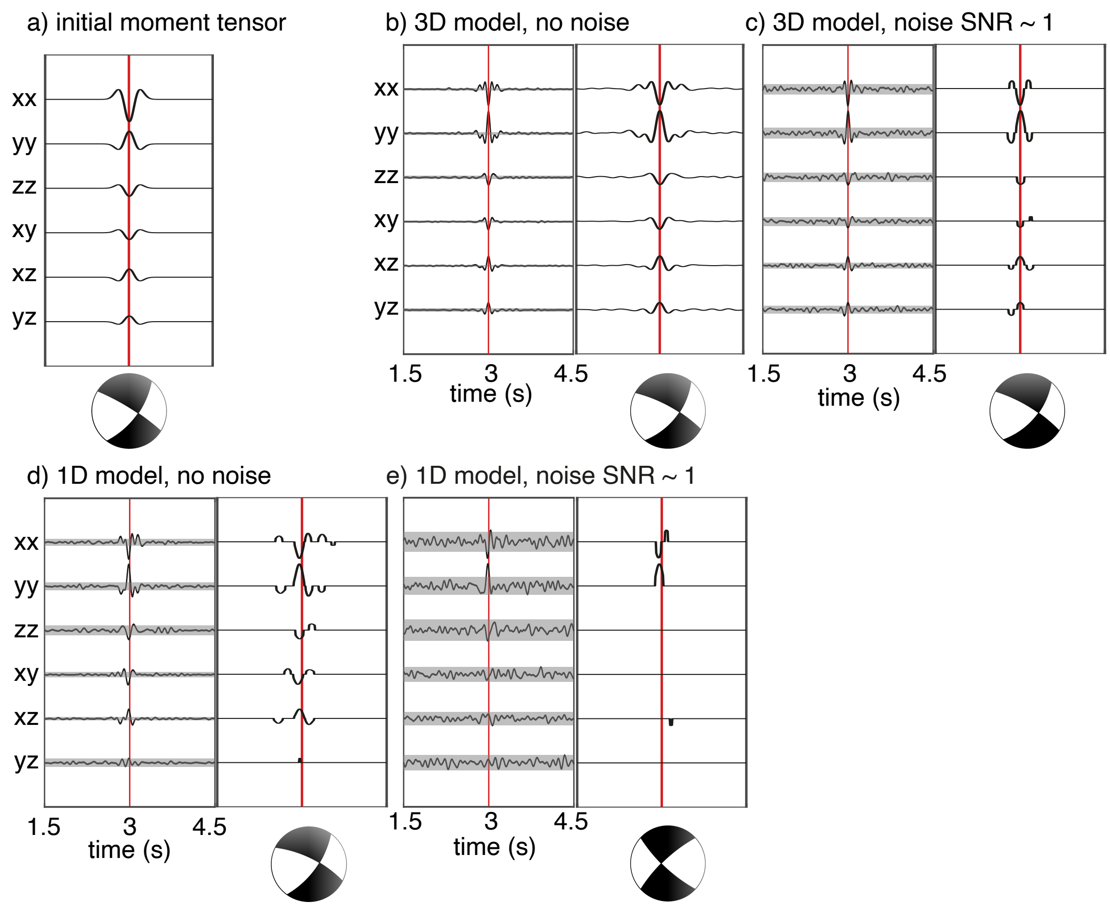

Figure 10: a) Initial moment tensor. b) to e) stress recorded at source location during reverse simulation for varying cases. The origin time is marked by a vertical red line. The noise level determined from the illumination map simulation is marked as a grey bar in the left plots for each case. In the right plots for each case, the time-dependent moment tensor is shown zoomed in and with supppressed noise. Focal Mechanism solutions were produced with the double-couple part of the obtained scalar moment tensor and using the code provided by Krieger and Heimann (2012).

Finger & Saenger – GEO-2020-0348

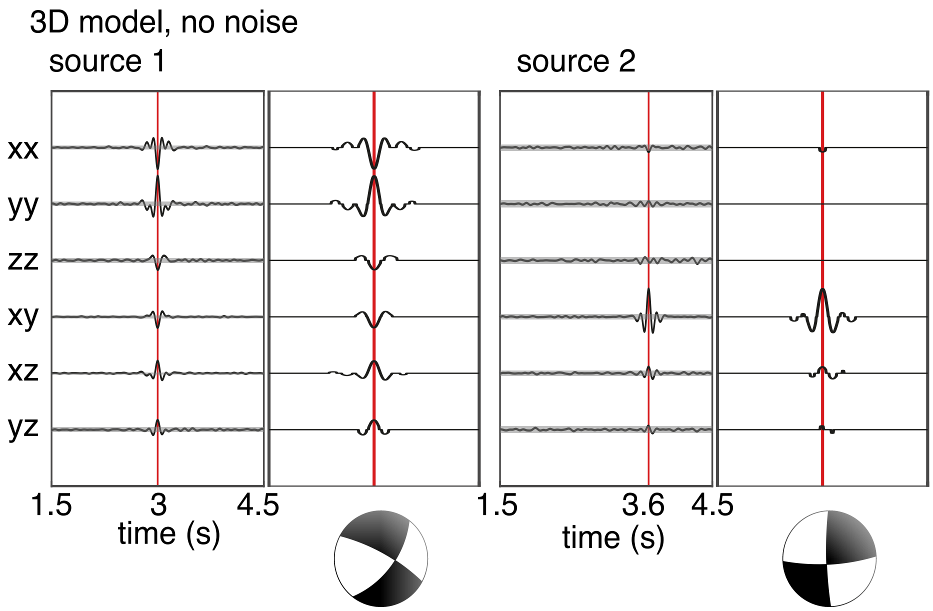

Figure 11: Characterization result for two synthetic sources with the three-dimensional model and without noise added to the displacement data. The origin time is marked by a vertical red line. The peak noise level of the stress traces is determined from the illumination map simulation and is marked as a grey bar in the left plots for each case. In the right plots for each case, the time-dependent moment tensor is shown zoomed in and with supppressed noise. Focal Mechanism solutions were produced with the double-couple part of the obtained scalar moment tensor and using the code provided by Krieger and Heimann (2012)

Finger & Saenger – GEO-2020-0348

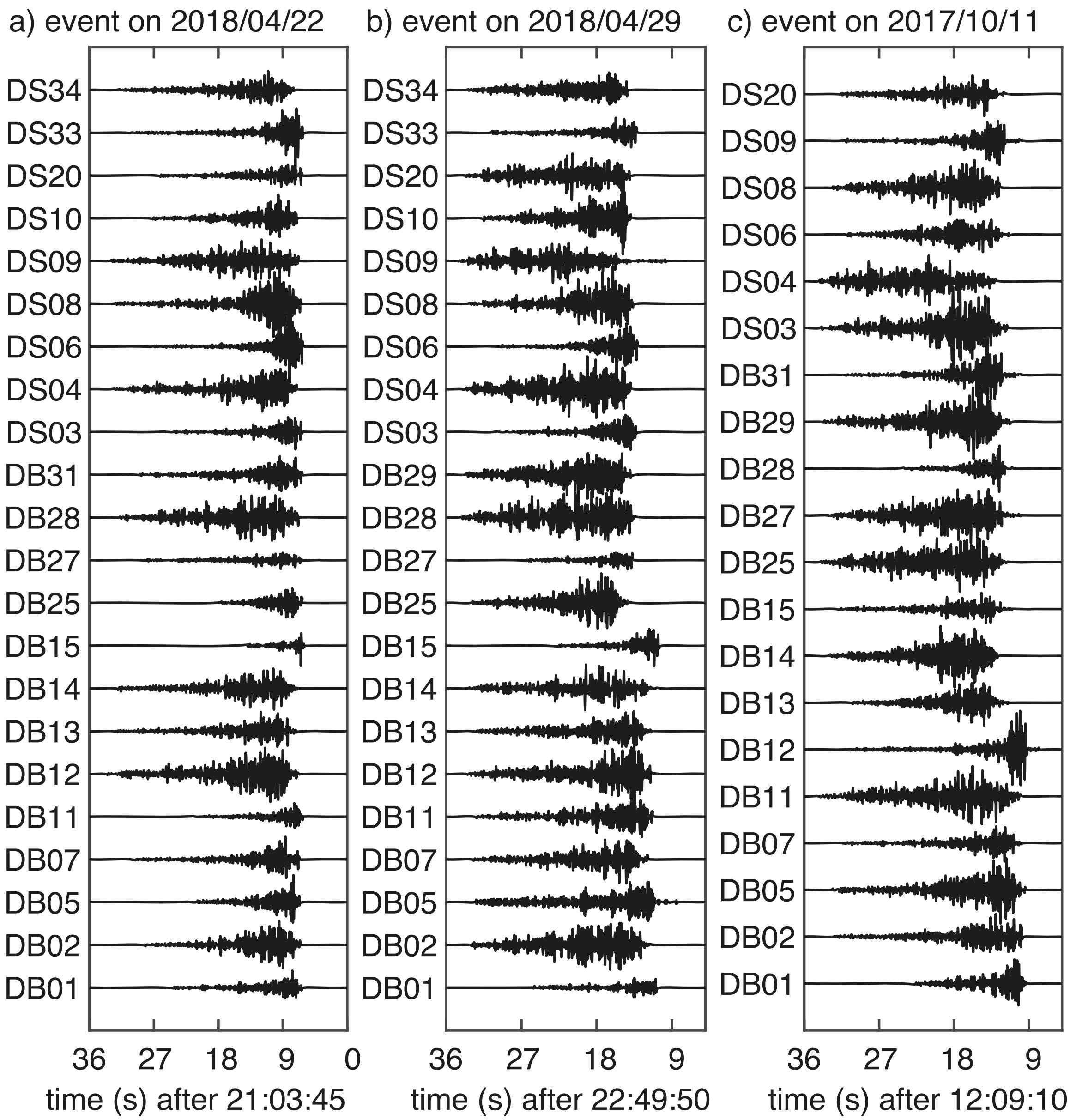

Figure 12: Vertical component of pre-processed (filtered between 2 Hz and 12 hz) and time-reversed displacement data from all available stations. a) Event recorded on 2018, April 22, b) event recorded on 2018, April 29 and c) event recorded on 2017, October 11.

Finger & Saenger – GEO-2020-0348

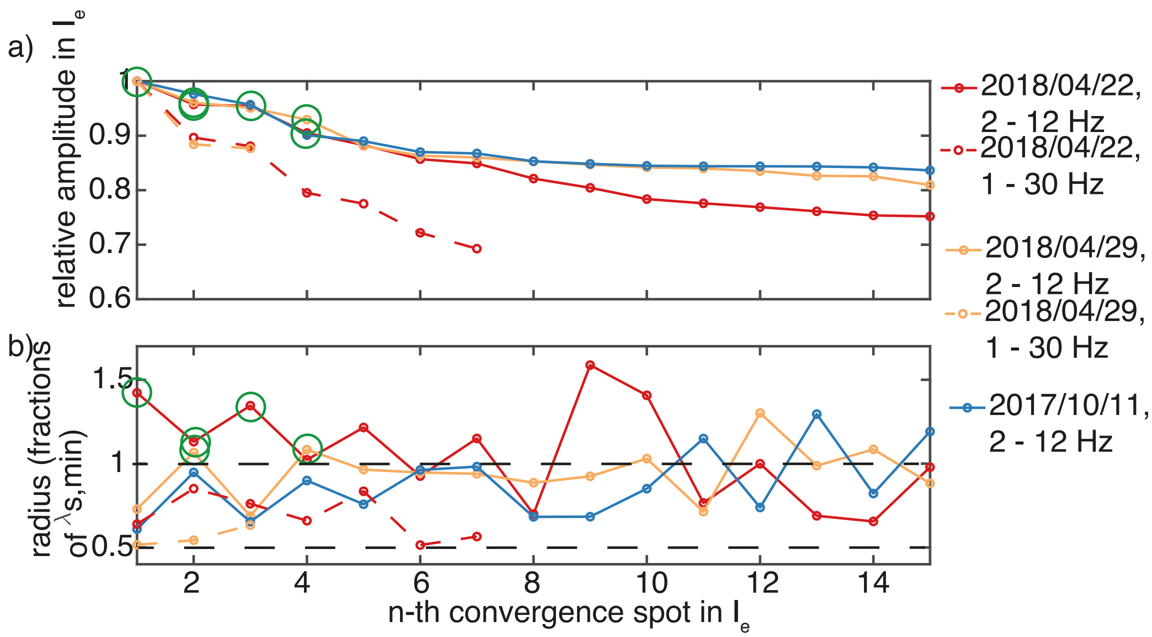

Figure 13: Characteristics of convergence locations for different microseismic events in two frequency bands. a) Amplitudes and b) radii of the 15 highest-amplitude convergence locations in $\mathbf{I}_{\mathrm{e}}$. Green circles mark convergence locations selected for analysis. Spots with a radius larger than $1\,\lambda_{\mathrm{S},min}$ were selected although the amplitude distribution did show as significant amplitude drops as in Figure 9.

Finger & Saenger – GEO-2020-0348

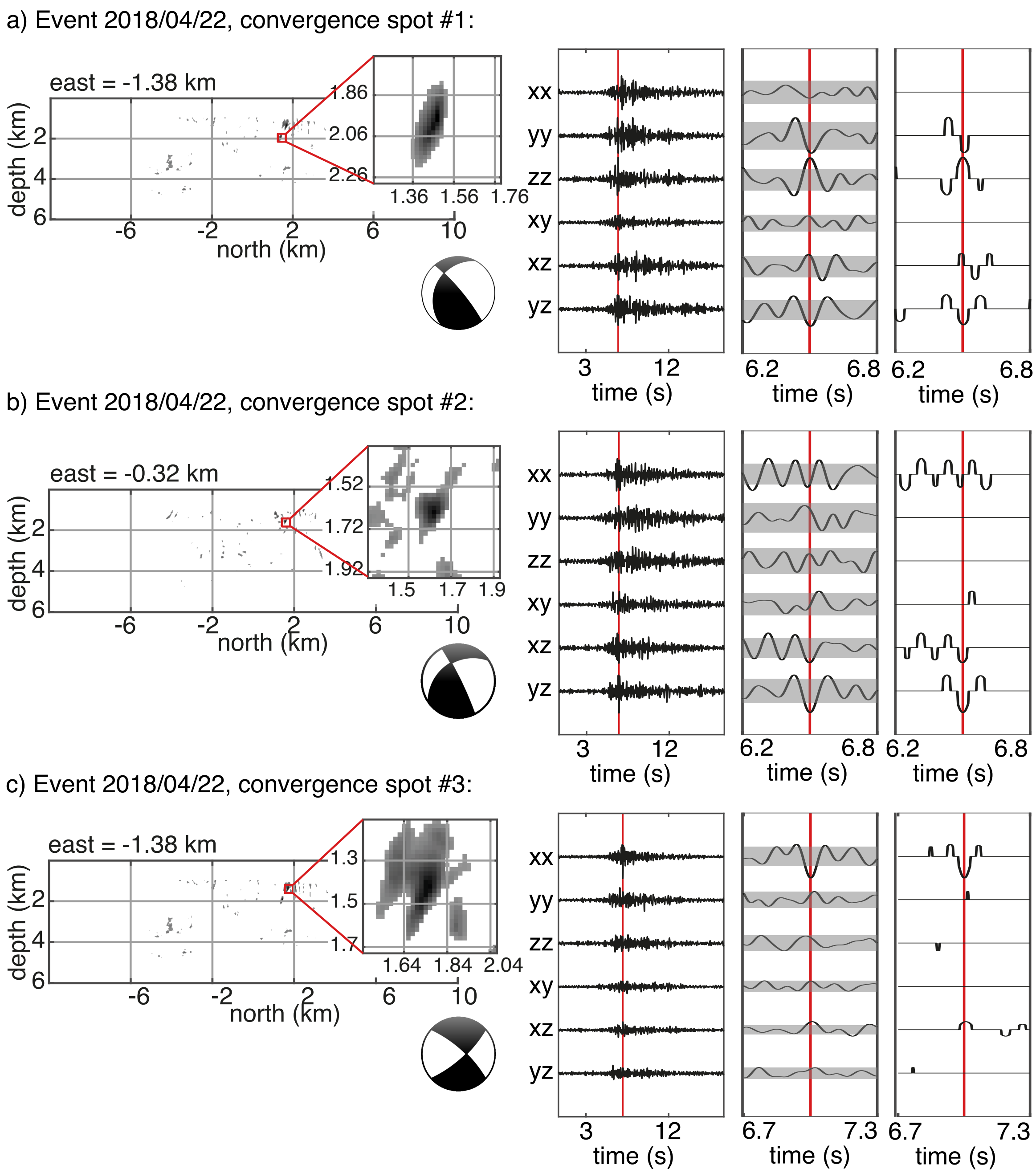

Figure 14: Location and characterisation results for the event on 2018, April 22. Convergence locations in $\mathbf{I}_{\mathrm{e}}$ with a radius larger than $1\lambda_{\mathrm{S},min}$ are compared.

Finger & Saenger – GEO-2020-0348

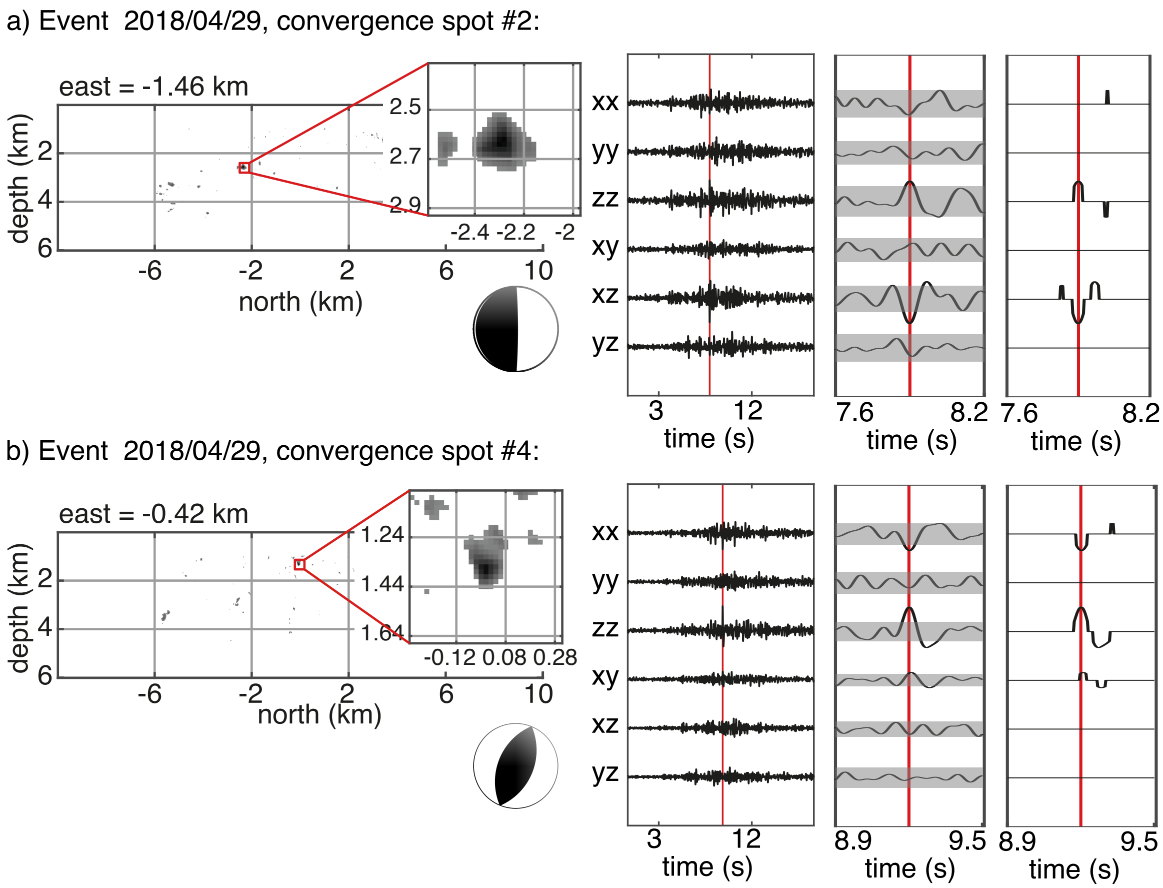

Figure 15: Location and characterisation results for the event on 2018, April 29. Convergence locations in I_e with a radius larger than $1\lambda_{\mathrm{S},min}$ are compared.

Finger & Saenger – GEO-2020-0348

Depth (km)	V_P (m/s)	V_S (m/s)
0 - 1	3330	1760
1 - 2	3600	2210
2 - 5.1	4460	2800
5.1 - 6	5860	3265

Table 1: One-dimensional velocity model derived from the three-dimensional realistic heterogeneous velocity model. This velocity model is used to demonstrated the influence of an incorrect velocity model.

Figure #	moment tensor components (xx, yy, zz, xy, xz, zy)	decomposition (ISO, DC, CLVD) in %	Fault plane 1 (strike, dip, slip-rake) in °	Fault plane 2 (strike, dip, slip-rake) in °
10a	-1, 0.57, -0.36, -0.31, 0.37, 0.26	21, 69, 10	37, 64, -170	302, 81, -26
10b	-0.74, 1, -0.34, -0.46, 0.43, 0.33	2, 90, 8	38, 60, -163	299, 75, -32
10c	-0.75, 1, -0.34, -0.28, 0.39, 0.31	2, 83, 15	40, 60, -164	302, 76, -31
10d	-0.76, 1, -0.4, -0.46, 0.43, 0.19	4, 84, 12	36, 66, -159	297, 71, -26
10e	-0.72, 1, 0, 0, -0.31, 0	9, 86, 5	133, 76, -15	227, 76, -165
11e	-0.76, 1, -0.33, -0.39, 0.44, 0.34	2, 92, 6	37, 60, -163	299, 76, -31
11e	-0.16, 0, 0, 1, 0.23, 0.14	4, 94, 2	87, 77, 172	179, 83, 13

Table 2: Derived scalar moment tensors, fault plane solutions and decomposition of moment tensor after Knopoff and Randall (1970). Plotted results and the time-dependent moment tensor are displayed in Figures 10 and 11.

Figure #	localisation (east, north, depth) in km	moment tensor (xx, yy, zz, xy, xz, zy)	ISO, DC, CLVD in %	Fault plane 1 (strike, dip, slip-rake) in °	Fault plane 2 (strike, dip, slip-rake) in °	origin time
14a	-1.38, 1.46, 1.96	0, 0.83, 1, 0, -0.64, -0.74	33, 49, 18	320, 80, 67	208, 25, 156	21:03:51.501
14b	-0.32, 1.6, 1.62	-0.74, 0, 0, 0.61, -0.7, -1	13, 9, 78	334, 84, 55	235, 35, 169	21:03:51.525
14c	-1.38, 1.74, 1.4	-1, 0, -0.36, 0, 0.37, 0	38, 16, 46	312, 73, -18	48, 73, -162	21:03:52.011
15a	-1.46, -2.3, 2.6	0.57, 0, 0.84, 0, -1, 0	27, 17, 56	180, 4, 90	0, 86, 90	22:49:57.926
15b	-0.42, -0.02, 1.34	-0.67, 0, 1, 0.32, 0, 0	10, 86, 4	22, 45, 90	202, 45, 90	22:49:59.183

Table 3: Derived scalar moment tensors, fault plane solutions, origin times and decomposition of moment tensor after Knopoff and Randall (1970). Plotted results and the time-dependent moment tensor are displayed in Figures 14 and 15.